

MICROCOPY RESOLUTION TEST CHART
NATIONAL BUREAU OF STANDARDS - 1963 - A

AD-A161 734

12

DNA-TR-85-8

MONTE CARLO CALCULATIONS ON THE DIRECT CABLE DRIVE DUE TO GAMMA RADIATION

Ed Kalasky
Mission Research Corporation
P.O. Drawer 719
Santa Barbara, CA 93012-0719

1 December 1984

Technical Report

CONTRACT No. DNA 001-81-C-0151

Approved for public release.
distribution is unlimited.

THIS WORK WAS SPONSORED BY THE DEFENSE NUCLEAR AGENCY
UNDER RDT&E RMSS CODE B326084466 X99QMXVC00021 H2590D.

DTIC FILE COPY

Prepared for
Director
DEFENSE NUCLEAR AGENCY
Washington, DC 20305-1000

DTIC
ELECTE
NOV 14 1985
B

85 10 8 080

Destroy this report when it is no longer needed. Do not return to sender.

PLEASE NOTIFY THE DEFENSE NUCLEAR AGENCY,
ATTN: STTI, WASHINGTON, DC 20305-1000, IF YOUR
ADDRESS IS INCORRECT, IF YOU WISH IT DELETED
FROM THE DISTRIBUTION LIST, OR IF THE ADDRESSEE
IS NO LONGER EMPLOYED BY YOUR ORGANIZATION.



REPORT DOCUMENTATION PAGE

1a REPORT SECURITY CLASSIFICATION UNCLASSIFIED		1b. RESTRICTIVE MARKINGS	
2a. SECURITY CLASSIFICATION AUTHORITY N/A		3. DISTRIBUTION / AVAILABILITY OF REPORT Approved for public release; distribution is unlimited.	
2b DECLASSIFICATION / DOWNGRADING SCHEDULE N/A since UNCLASSIFIED		5. MONITORING ORGANIZATION REPORT NUMBER(S) DNA-TR-85-8	
4 PERFORMING ORGANIZATION REPORT NUMBER(S) MRC-R-835		7a NAME OF MONITORING ORGANIZATION Director Defense Nuclear Agency	
6a NAME OF PERFORMING ORGANIZATION Mission Research Corp.	6b OFFICE SYMBOL (if applicable)	7b. ADDRESS (City, State, and ZIP Code) Washington, D.C. 20305-1000	
6c. ADDRESS (City, State, and ZIP Code) P.O. Drawer 719 Santa Barbara, CA 93102-0719		9. PROCUREMENT INSTRUMENT IDENTIFICATION NUMBER DNA 001-81-C-0151	
8a. NAME OF FUNDING / SPONSORING ORGANIZATION	8b OFFICE SYMBOL (if applicable)	10 SOURCE OF FUNDING NUMBERS	
8c. ADDRESS (City, State, and ZIP Code)		PROGRAM ELEMENT NO 52715H	PROJECT NO X99QMXV
		TASK NO C	WORK UNIT ACCESSION NO DH008508
11 TITLE (Include Security Classification) MONTE CARLO CALCULATIONS ON THE DIRECT CABLE DRIVE DUE TO GAMMA RADIATION			
12 PERSONAL AUTHOR(S) Ed Kalasky 30 June 1984 thru 1 Aug. 1984			
13a TYPE OF REPORT Technical	13b TIME COVERED FROM 840801 TO 840630	14 DATE OF REPORT (Year, Month, Day) 841201	15 PAGE COUNT 76
16 SUPPLEMENTARY NOTATION This work was sponsored by the Defense Nuclear Agency under RDT&E RMSS code B326084466 X99QMXVC00021 H2590D.			
17 COSATI CODES		18 SUBJECT TERMS (Continue on reverse if necessary and identify by block number)	
FIELD	GROUP	IEMP Cable SGEMP	
20	8	Direct Drive Compton Electrons	
20	14	Gamma Radiation Monte Carlo Calculations	
19 ABSTRACT (Continue on reverse if necessary and identify by block number) Two Monte Carlo codes, labeled MCABLE and MCIMP, were developed to determine the direct drive currents in cables due to gamma radiation. MCABLE was written in cylindrical coordinates for circular shaped cables and MCIMP in Cartesian coordinates for any arbitrary shape. A background into single and multiple scattering theory with an emphasis on the Moliere and Scott-Snyder distribution functions is presented. Range and emission current calculations are provided to substantiate the validity and accuracy of the technique used in the Monte Carlo codes. An experimental comparison was also made to verify the accuracy of the codes. A parametric study was conducted on the response of a coaxial cable due to variations in the dimensions and material types. Based on this study, a simple model for estimating the shield and center conductor currents is presented. Finally, a comparison is made between the response of eight cables measured in the laboratory and the Monte Carlo code MCABLE.			
20 DISTRIBUTION / AVAILABILITY OF ABSTRACT <input type="checkbox"/> UNCLASSIFIED/UNLIMITED <input checked="" type="checkbox"/> SAME AS RPT <input type="checkbox"/> DTIC USERS		21 ABSTRACT SECURITY CLASSIFICATION UNCLASSIFIED	
22a NAME OF RESPONSIBLE INDIVIDUAL Betty L. Fox		22b. TELEPHONE (Include Area Code) (202) 325-7042	22c. OFFICE SYMBOL DNA/STTI

TABLE OF CONTENTS

<u>Section</u>		<u>Page</u>
	TABLE OF CONTENTS	i
	LIST OF ILLUSTRATIONS	ii
	LIST OF TABLES	iii
1	INTRODUCTION	1
2	THE MONTE CARLO CODE VERIFICATION AND RESULTS	7
	2.1 Validation Checks	13
	2.2 Experimental Check	18
	2.3 Parametric Studies	19
	2.4 Aspects of Modeling	27
	2.5 Results	32
3	CONCLUSIONS	36
	REFERENCES	38
	APPENDIX	
	Single and Multiple Scattering Theory	A-1



Accession For	
NTIS GRA&I	<input checked="" type="checkbox"/>
DTIC TAB	<input type="checkbox"/>
Unannounced	<input type="checkbox"/>
Justification	
By	
Distribution/	
Availability Codes	
Dist	Avail and/or Special
A-1	

LIST OF ILLUSTRATIONS

<u>Figure</u>		<u>Page</u>
1	An example of 4 gamma rays penetrating a triaxial cable creating internal currents by ejecting one "weighted" electron per gamma ray.	2
2	The equipotential lines in the MX cable labeled #1.	4
3	The shield, dielectric, and center conductor "currents" J in (coul/m)/(cal/cm) as determined from the Monte Carlo code MCABLE and their ratio to the net current J_N as a function of size of the center conductor.	20
4	The shield, dielectric, and center conductor "currents" J (coul/m)/(cal/cm) as determined from the Monte Carlo code MCABLE and their ratio to the net current J_N as a function of the shield thickness.	21
5	The shield, dielectric and center conductor "currents" (coul/m)/(cal/cm) as determined from the Monte Carlo code MCABLE and their ratio to the net current as a function of various material types as labeled in Figures a through d.	23
6	The shield, dielectric, and center conductor "currents" (coul/m)/(cal/cm) as determined from the Monte Carlo code MCABLE and their ratio to the net current as a function of the shield thickness for two different sets of material.	24
7	The shield, dielectric, and center conductor "currents" (coul/m)/(cal/cm) as determined from the Monte Carlo code MCABLE and their ratio to the net current as a function of two different dielectric materials with and without an air gap.	26
8	The shield, dielectric, and center conductor "currents" (coul/m)/(cal/cm) and their ratio to the net current for various cables tested.	33

LIST OF ILLUSTRATIONS (Concluded)

<u>Figure</u>		<u>Page</u>
9	This is a comparison between measured in air (M) and calculated (C) responses of 8 cables using the computer code MCABLE.	34

LIST OF TABLES

<u>Table</u>		<u>Page</u>
1	Computer Range Checks.	15
2	Computer Emission Current Checks.	17
3	The results of a simple analytical model are compared to those of the Monte Carlo code MCABLE.	31

SECTION 1 INTRODUCTION

The response of a cable due to the interaction of γ rays is dependent on the geometry of the cable, the materials used, and the construction of the cable. In this report we will look at some of the different aspects of a computer code for calculating the short circuit current response of a cable, various computer and experimental checks, a parametric study, and a comparison between the measured cable responses and the predicted values. But first, let us summarize some of the physical concepts behind the generation of the currents known as direct cable drive.

When γ rays pass through matter they lose some or all of their energy in discrete events producing photoelectrons, Compton electrons and possibly, if their energy is sufficient, they will produce both an electron and a positron in an event called pair production. Although this latter event will not contribute any net current to the cable, it can reduce the probability of producing a Compton electron. So let us now look at the physical process that takes place when a uniform flux of monoenergetic gamma rays pass through a cable as depicted in Figure 1. The gamma rays in this figure are represented by a series of random straight lines crossing the triaxial cable. Since we will assume that the cable is thin with respect to the mean free pathlength of the gamma rays, we will not consider secondary scattering of the photons within the cable. The random direction of the gamma rays in Figure 1 simulates a twisted cable, which, in this case, consists of an outer shield, three inner conductors, each surrounded by a dielectric, and packed together with a filler material. As each gamma ray penetrates the cable it may, or may not, create an electron.

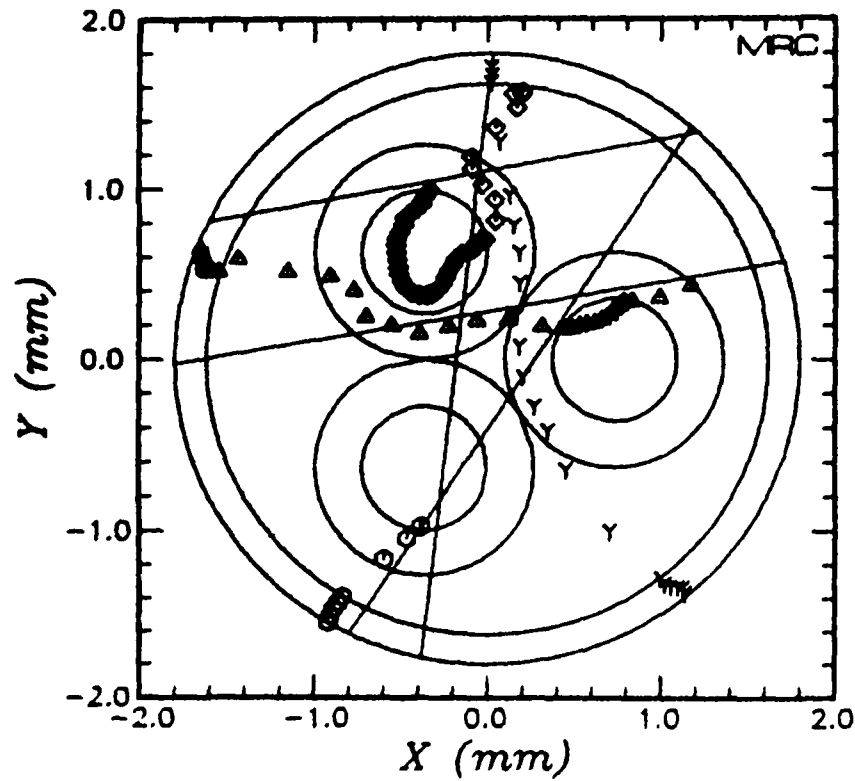


Figure 1. An example of 4 gamma rays penetrating a triaxial cable creating internal currents by ejecting one "weighted" electron per gamma ray. The gamma rays are designated by straight lines crossing the cable and the electron paths by various special characters. Each inner conductor is surrounded by a dielectric material packed in a filler within the outer (ring) shield.

The probability of creating a single electron by any given gamma ray is related to the density of the material, the pathlength through each substance, and the energy of the gamma ray. Using this information we can determine the pathlength of each gamma ray across the cable in fractions of its mean free pathlength. Based on this length, the exponential attenuation function for the photon is computed and compared to a random number between zero and one. If the attenuation function is greater than the random number, scattering or photon absorption would occur within the cable at the position determined by the random number. In Figure 1, we see the trajectory of the four gamma rays crossing the cable and the paths of four electrons, represented by the four special characters, each originating on the path of a gamma ray. Although there is an electron associated with each gamma ray in Figure 1, the probability of creating an electron per gamma ray in the cable is usually much less than one. Therefore, we can either keep picking random numbers until an electron is created within the cable or we can create an electron per gamma ray by selecting an appropriate compensating "weight" for each electron. Mathematically, we will achieve the same end result in determining the net current in the cable. However, the latter method will save some computer time.

Once an electron is created, it is moved according to the classical equations of motion and scattered according to the Snyder-Scott distribution function. The magnitude of the sequential steps of each electron, as shown in Figure 1 by the special characters, is based on the electron density of the material and the energy of the electron. The actual amount of current or charge per calorie of gamma rays generated by the displaced electrons within a cable is determined by the amount of induced image charge on the opposing conductor. Since the induced charge is proportional to the change in an electron's potential, we can determine the induced charge as the potential difference between the initial and final states of the electron times its charge by setting the potential on the inner conductor to zero and one on the shield. In Figure 2 we show

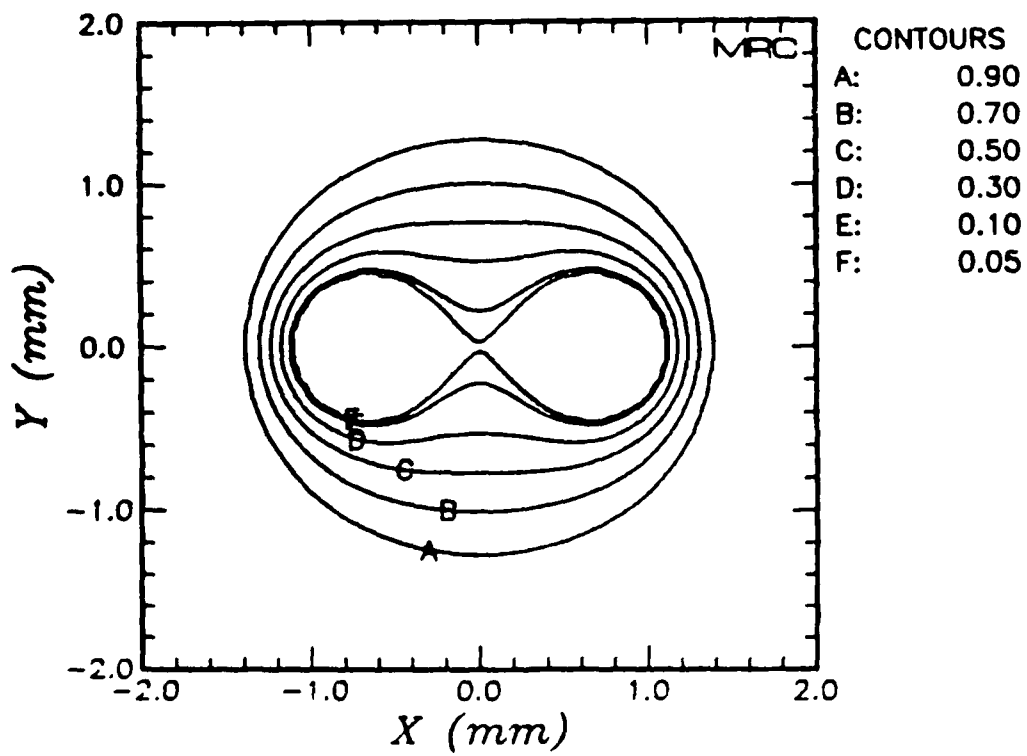


Figure 2. The equipotential lines in the MX cable labeled #1. A cross section of the MX cable, which contains two inner conductors, is shown in Figure 8.

the equipotential lines for a twin axial cable. The amount of induced charge by a single electron which travels from the equipotential line A to B would be equaled to 0.2 times an electron's charge.

Low energy photons, such as x-rays, are very effective in producing a net flow of electrons from the shield towards the center conductors by way of the photoelectric effect. When a thin material sample is exposed to these photons, they generate large electron emissions both in the forward and backward directions due to their interaction with the electrons in the sample. Although this interaction enhances the generation of electrons, it also reduces the photons ability to penetrate the sample. This makes it relatively easy to provide effective shielding against these photons. As the energy of the photons is increased, the dominant physical process for creating free electrons changes from the photoelectric effect to Compton scattering, in which a photon imparts energy into an electron during a collision. These two processes are equally probable in aluminum when the energy of the photon equals 50 Kev and in copper at 0.5 Mev. The mean attenuation lengths of these photons are 1.0 and 1.3 centimeters in their respective materials. Due to these longer attenuation lengths it becomes more difficult to shield cables against these photons. However, they are also less likely to interact with a particular cable due to their capability of penetrating the cable so easily. In addition, whenever the attenuation lengths are larger than the diameter of the cable, these photons will also have a tendency to create as many electrons from the shield as from the center conductors resulting in smaller net transfer of charge. As the energy of the photons is increased further to high energy gammas, 5 Mev and above, the efficiency of inducing a current in a cable is further reduced not only due to their ability to penetrate the cable, but also, due to the third physical process of interaction called pair production. The mean attenuation length of a 5 Mev photons in copper is 3.5 cm and 13.0 cm in aluminum.

Therefore, depending on one's objective it is possible to either design a cable with shielding which will produce a minimum response to a given photon spectrum or to design a spectrum which will maximize the current response from a particular shielded cable.

SECTION 2 THE MONTE CARLO CODE VERIFICATION AND RESULTS

In this section we discuss the computer codes and validation checks, an experimental verification, a set of parametric studies, some preliminary remarks on cable modeling, and provide a comparison of the calculated and measured responses to a set of cables. There are two basic computer codes. One determines the potential gradient in a cable or grid and the other, based on this gradient, determines the response of that cable or box structure in terms of electrons per unit energy. The first code determines the equipotential lines as shown in Figure 2 by solving Poisson's equation in two dimensions and in Cartesian coordinates. From Maxwell's first law of electromagnetism, we can write

$$\vec{\nabla} \cdot (K \nabla \phi) = K \nabla^2 \phi + \nabla K \cdot \nabla \phi = -\rho / \epsilon_0 \quad (1)$$

where $K = \epsilon / \epsilon_0$

In Cartesian coordinates, we have

$$\left(\frac{\partial^2 \phi}{\partial x^2} + \frac{\partial^2 \phi}{\partial y^2} \right) + \frac{\partial K}{\partial x} \frac{\partial \phi}{\partial x} + \frac{\partial K}{\partial y} \frac{\partial \phi}{\partial y} = -\rho / \epsilon_0 \quad (2)$$

We solve this equation by the method of successive over-relaxation (SOR) using the accelerated Gauss-Seidel formulation.¹ The basic idea is to replace Poisson's equation with a diffusion equation

$$\frac{\partial u}{\partial t} - \nabla^2 u = \rho \quad (3)$$

and let our potentials diffuse into a steady state condition given the boundary conditions (zero potential on the shield and unity on the center conductors). The Gauss-Seidel technique specifies the optimum value of ω for each successive iteration in order to achieve a steady state solution. The computer codes PISC and PISA take less than one minute to solve a 51 by 51 grid pattern and a little more than a minute for a 101 by 101 grid pattern on the VAX780. The input to PISC is in cylindrical coordinates for pre-defined cable geometries, whereas, PISA will solve any arbitrary geometry.

The Monte Carlo cable codes are called MCABLE and MCIMP. MCABLE is written in cylindrical coordinates and MCIMP is written in Cartesian coordinates. The MCABLE code assumes that the cross section of conductors, as shown in Figure 1, are circular. Therefore, one must specify the number of center conductors, their locations, the radius of the center conductors, dielectric insulators, the filler material, the radius of an air gap if there is one, and the radius of the shield. Of course, one must also specify the material types used in each region. In the MCIMP code any cable or arbitrary structure is subdivided into a grid pattern (typically 100 by 100), in which, each cell must be specified with a given material type. Although this may sound like an unforgiving burden, the format is such that a partial or complete row or column can be assigned to a given material type very easily. This code is particularly useful for making computer checks and calculating the response of flat or non-symmetrical cables.

Although there are small differences in the logic between the two codes MCABLE and MCIMP, the same physical principles are used in both programs. The probability of producing an electron from a gamma ray is obtained by the ratio of the sum of the photoelectric and Compton cross sections to the total cross section including pair production times its "weighted" probability that it will be absorbed or scattered in the given thickness of the cable under consideration. As the gamma ray passes

through several different material types the appropriate cross sections for each material is used. The cross sections for each of these three processes are directly related to the atomic number and inversely proportional to the atomic weight of the material.² In the Monte Carlo codes these cross sections are determined from the following equations

$$\sigma_{PE} = \sigma_{PEa} \frac{A_a}{A} \left(\frac{Z}{Z_a}\right)^{4.6} \quad (4)$$

$$\sigma_C = \sigma_{Ca} \frac{A_a}{A} \frac{Z}{Z_a} \quad (5)$$

$$\sigma_{PP} = \sigma_{PPa} \frac{A_a}{A} \left(\frac{Z}{Z_a}\right)^2 \quad (6)$$

where σ_{PEa} , σ_{Ca} and σ_{PPa} are the photoelectric, Compton and pair production cross sections for air as determined explicitly in the program. A_a and Z_a are the weighted average numbers for the atomic weight (14.4) and number (7.2) of air.

For 1 Mev photons the vast majority of electrons will be created by Compton scattering. The Klein-Nishina cross section for photons was used with its corresponding distribution for the ejected electrons. The angle of the ejected electron with respect to the gamma ray's path is determined by subdividing the Klein Nishina cross section into equally probable fractions of the total cross section (typically 200). A random number generator is then used to select an appropriate fraction from which the scattering angle of the electron is determined. A simple transformation from the gamma's path to the Monte Carlo coordinate system creates the new electron with a specified energy and direction. The electron's position is recorded both in terms of its coordinates and in terms of the

potential function described above, since the induced current is proportional to the potential difference each electron transverses.

The electron moves through the cable according to the classical equation of motion and is scattered according to Snyder-Scott distribution as outlined in Appendix A. The equation of motion for the electron is given by

$$\frac{d\vec{p}}{ds} = - A(\epsilon) \frac{\vec{p}}{|\vec{p}|} \quad (7)$$

where $A(\epsilon)$ is the drag factor in Bethe's formula and is approximated by the following:³

$$A(\epsilon) \approx 2\pi NZ r_0^2 \left(\frac{\epsilon}{p}\right)^2 \left(2.0 \ln \left(\frac{mc^2}{I}\right) + 3.42 \ln(p) - 1.71\right)$$

where ϵ and p are the energy and momentum of the electron in electron rest mass units, I is the mean excitation potential, r_0 is the classical electron radius, and N is the density of atoms with an atomic number of Z . Although the step size ds in the equation of motion is restricted to changes in momentum of less than FACP (typically 10%), we must select a step size between scattering events which will be used in the Snyder-Scott distribution. We have found through experience with the Snyder-Scott distribution that we can achieve the same results with an interval step size which yields an average of 10 or more scatterings per electron pathlength as one obtains using 100 scatterings per pathlength. This was accomplished by subdividing the step size such that the mean number of collision per unit pathlength remained the same (ρ_0 see the theory section in the Appendix) whenever the momentum of the electron dropped below an input parameter HAP. This procedure ensures us of good statistics for the low

energy electrons and increases our efficiency in obtaining the results quickly. Typically, 4,000 to 10,000 particles per photon energy bin are required depending on the material types and the geometry of the cable, since electrons which do not leave either conductor do not contribute to the statistics of determining the net flow of current. It takes roughly one minute to process a thousand electrons on the VAX780.

The electron scattering angle is determined from the Snyder-Scott projected distribution in the following manner. The probability of getting a deflection of any angle θ_R in the projected plane is determined by the equation:

$$P = \lim_{\theta_E \rightarrow \infty} \frac{\int_0^{\theta_R} d\theta'_R W(\theta'_R, \Omega_0)}{\int_0^{\theta_E} d\theta'_R W(\theta'_R, \Omega_0)} \quad (8)$$

where P is a generated random number between zero and one, and $W(\theta_R, \Omega_0)$ is the Snyder-Scott distribution.

$$W(\theta_R, \Omega_0) = A_1 e^{-a_1 \theta_R^2} + A_2 e^{-a_2 \theta_R^2} \quad (9)$$

for $W > .007 W(0, \Omega_0)$ and

$$W(\theta_R, \Omega_0) = \frac{\Omega_0}{2\theta_R^3} \left\{ 1 + \frac{11.68\Omega_0 \log(10\Omega_0)}{\theta_R^2} \right\} \quad (10)$$

for $W < .007 W(0, \Omega_0)$. θ_R is called the reduced angle in the projected plane since it is in units of the Moliere screening angle χ_m , that is, $\theta_R = \theta_p / \chi_m$ (see the theory section in the Appendix). Ω_0 is a function of the size step ds and can be thought of as the mean number of scattering an

electron would encounter in length ds . The spatial angle is then computed as $\sqrt{2}$ times the projected angle θ_p and the azimuthal angle ϕ is determined by another random number between zero and 2π .

We have now covered all of the essential ingredients of the Monte Carlo code. The induced currents are calculated in the MCIMP code as

$$J(\text{coul/cal}) = \frac{e \sum_j (\phi_f - \phi_i)_j w_j}{N_Y E_Y 3.827E-14 \text{ cal/Mev}} \quad (11)$$

where N_Y = number of gamma rays
 E_Y = energy of the gamma rays in Mev
 e = the electron charge
 w_j = "weight" or current contribution factor
 ϕ_i = the initial potential state of the electron
and ϕ_f = the final state,

or as

$$J(\text{coul/m})/(\text{cal/cm}^2) = \frac{N_Y e \sum_j (\phi_f - \phi_i)_j w_j (100/XL)}{(N_Y/XL)^2 E_Y 3.827E-14 \text{ cal/Mev}} \quad (12)$$

where XL = X-dimension of box in centimeters

$(N_Y/XL)^2$ = gamma fluence

$$J(\text{coul/m})/(\text{cal/cm}^2) = J(\text{coul/cal}) * (100XL)$$

In the MCABLE code

$$J(\text{coul/m})/(\text{cal/cm}^2) = \frac{N_Y e \sum_j (\phi_f - \phi_i) w_j (100/(2R_s))}{(N_Y/(2R_s))^2 E_Y 3.827E-14 \text{ cal/Mev}} \quad (13)$$

where R_s = radius of the shield in centimeters.

2.1 Validation Checks

Two sets of validation checks were performed to verify the method and accuracy of the Monte Carlo calculation. In the first case, the mean electron range in various materials for several different energies were determined to verify the accuracy of using the Scott-Snyder distribution function. In the second case, the forward and backward emission currents were determined to ensure that the proper "weight" or current contribution per electron had been determined. The ranges were determined for both the forward directed and Compton electrons using a mode of operation called single point emission within a parallel plate capacitor. In this mode, all of the electrons are "born" at a designated spot with either their momentum directed forward or with a Klein-Nishina distribution directed towards one of the plates of the parallel plate capacitor. Since the potential differences in a parallel plate capacitor with a single dielectric constant are directly proportional to the distance between the plates, the mean, forward and backward electron ranges were computed by converting the average potential differences for each of the three functions directly into ranges. The results are listed in Table 1 and the ranges of the forward directed electrons are compared to the results from the Handbook of Photo-Compton Current Data.⁴ The results of the MCIMP code are in good agreement with the Photo Compton Handbook except for polyethylene. This can be attributed to the fact that we followed the procedure of Longmire¹⁶ and treated CH_2 as an element of

atomic number 8 and atomic weight of 14 rather than combining the elements in the compound by weight as done for teflon ($-CF_2-$) and other compounds. In order to show the effect of doubling the number of collisions per pathlength, the ranges for an electron created by a 5 Mev gamma ray were computed with 19 collisions per pathlength and 38 collisions per pathlength yielding mean ranges of 3.56 mm and 3.46 mm in aluminum. The computer's run time is directly proportional to the number of collisions per pathlength and doubled in this comparison. (The large variation in the backward compton electron ranges at 5 Mev is due to poor statistics.)

Table 1. Computer Range Checks. The mean, forward and backward electron ranges as determined from the Monte Carlo code MCIMP for various materials and energies versus the mean range values as published in the Handbook of Photo-Compton Current Data. All ranges are listed in millimeters and the average number of scatterings (ANS) used to determine these ranges in MCIMP is also listed.

Gamma Ray Energy (Mev)	Material Type	Mean Electron Energy (Mev)	Photo-Compton HDBK		MCIMP Code			
			Mean Range (mm)	Mean Range (mm)	Compton Electrons			ANS
					Mean Range (mm)	Forward Range (mm)	Backward Range (mm)	
1/2	Aluminum	.170	.055	.052	.091	-.0405	18.1	
1	Copper	.441	.046	.055	.075	-.0235	25.5	
	Aluminum	.446	.246	.241	.324	-.0734	26.4	
	Teflon	.440	.365	.365	.481	-.139	12.0	
	Polyethylene	.444	.936	.727	1.056	-.346	12.5	
5	Aluminum	3.18	3.38	3.46	3.74	-.330	43.1	
		3.18	3.38	3.56	3.74		21.9	
		3.26	3.48					

The second set of validation checks involved verifying the forward and backward emission currents as calculated by the Monte Carlo code. This was done indirectly since the electrons which flow from the upper plate of the parallel plate capacitor into the dielectric material are multiplied by the potential difference they transverse. Therefore, the average potential difference or range was used to compute the forward emission current. The same logic is true at the lower plate of the capacitor in order to compute the backward emission current. In both of these validation checks the material which is referred to as the dielectric material can be substituted with any other material. Since we are solving mathematical equations, we are not bounded by certain physical limiting realities, such as, substituting in a good conductor like aluminum or copper for our dielectric material. However, we must not overlook any physical principles which do apply, such as the steady state flow of electrons determining the emission currents. In this case, the upper and lower plates of the parallel plate capacitor *must be sufficiently thick to ensure that a steady state of electron flow has been established across the boundaries with the "dielectric" material.* This requires that the top plate, which is receiving the gamma radiation, be at least 4 or 5 electron mean free pathlengths thick and the bottom plate at least 2 or 3 mean free pathlengths. The results of the emission current calculations are listed in Table 2. The agreement is very good except for the 5 Mev case where the comparison values were determined from the Photo-Compton Handbook instead of from QUICKE2.⁵ (QUICKE2 is a later version of QUICKE which was used to determine the values published in the Photo-Compton Handbook.) The backward emission currents for this case were not listed in Table 2, since there was an order of magnitude difference between the projected values from QUICKE2 and the values published in the handbook.

The values determined from the Photo-Compton Handbook and for the backward emission currents from QUICKE2 have tended to be high. Therefore, values were selected from Chadsey's "X-Ray Photoemission"

Table 2. Computer Emission Current Checks. J_F and J_B are the forward and backward emission currents as determined from QUICKE2 for E equaled to 1/2 and 1.0 Mev and from the Photo-Compton Handbook for the 5 Mev case. The second set of numbers for E equaled to 1/2 and 1.0 Mev are from the Chadsey's report on "X-ray Photoemission."

E Mev	J_F Coul/cal	MCIMP Coul/cal	Material Type	J_B Coul/cal	MCIMP Coul/cal
1/2	1.25E-8 1.22E-8	1.28E-8	Copper	-3.05E-9 -2.20E-9	-1.12E-9
1/2	1.50E-8 1.30E-8	1.04E-8	Aluminum	-1.70E-9 -1.07E-9	-5.33E-10
1	1.88E-8 1.67E-8	1.49E-8	Copper	-3.70E-9 -2.20E-9	-2.79E-9
1	2.00E-8 1.99E-8	1.75E-8	Aluminum	-2.00E-9 -1.15E-9	-1.42E-9
5	1.77E-8	1.08E-8	Copper		-6.38E-10
5	2.12E-8	1.43E-8	Aluminum		-2.29E-10

report , in which, he compares the computer codes QUICKE2 and POEM to some very limited data measurements in this region of 1/2 and 1 Mev. Since Chadsey shows that the computer code POEM gives better results for the backward emission currents, we have listed those values in Table 2. However, we cannot explain the discrepancy between Chadsey's and Savage's values for the forward emission currents obtained from QUICKE2 at 1/2 Mev for aluminum and 1 Mev for copper. This only helps to emphasize the point that we should be comparing our emission currents against measured values and not other computer codes. Based upon the excellent agreement we obtained in Table 1 for the mean ranges, we might have expected almost exact agreement with the forward emission currents in the 1 Mev case in particular, since the backward emission currents agree. These discrepancies should be resolved with experimental data.

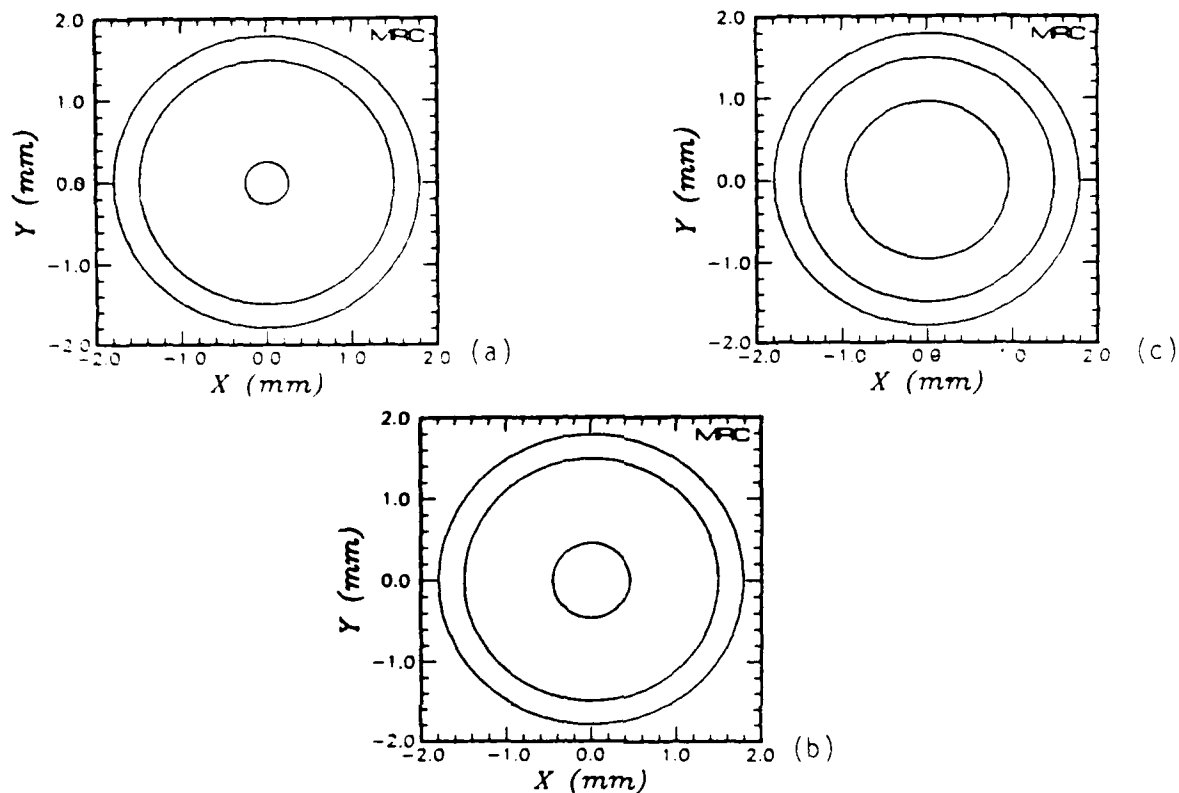
2.2 Experimental Check

In addition to these validation checks, an experimental verification check was performed by using a device which is called a solid photo-emission diode (SPED). This device consists of three parallel plates buried within a block of polyethylene in a sandwich layered construction. The two outer plates were made of 10 mil aluminum and electrically grounded, while the inner plate was made of copper 1/16 of an inch thick. The separation thickness between the plates consisted of 1/4" of polyethylene. During the assembly of this device, an attempt was made to eliminate any air gaps by heating the device causing the polyethylene to soften and hopefully fill the gaps. This attempt was apparently unsuccessful since the measured response was positive in air and negative in a vacuum. The vacuum response of $-2.79\text{E}-9$ coul/cal did agree very well with the computed value of $-3.0\text{E}-9$ coul/cal from the Monte Carlo code MCIMP using an average gamma ray energy of 1.1 Mev. Unfortunately, it is only of limited usefulness in verifying the accuracy of the Monte Carlo codes due to the possibility of stored charge being released during the measurement.

2.3 Parametric Studies

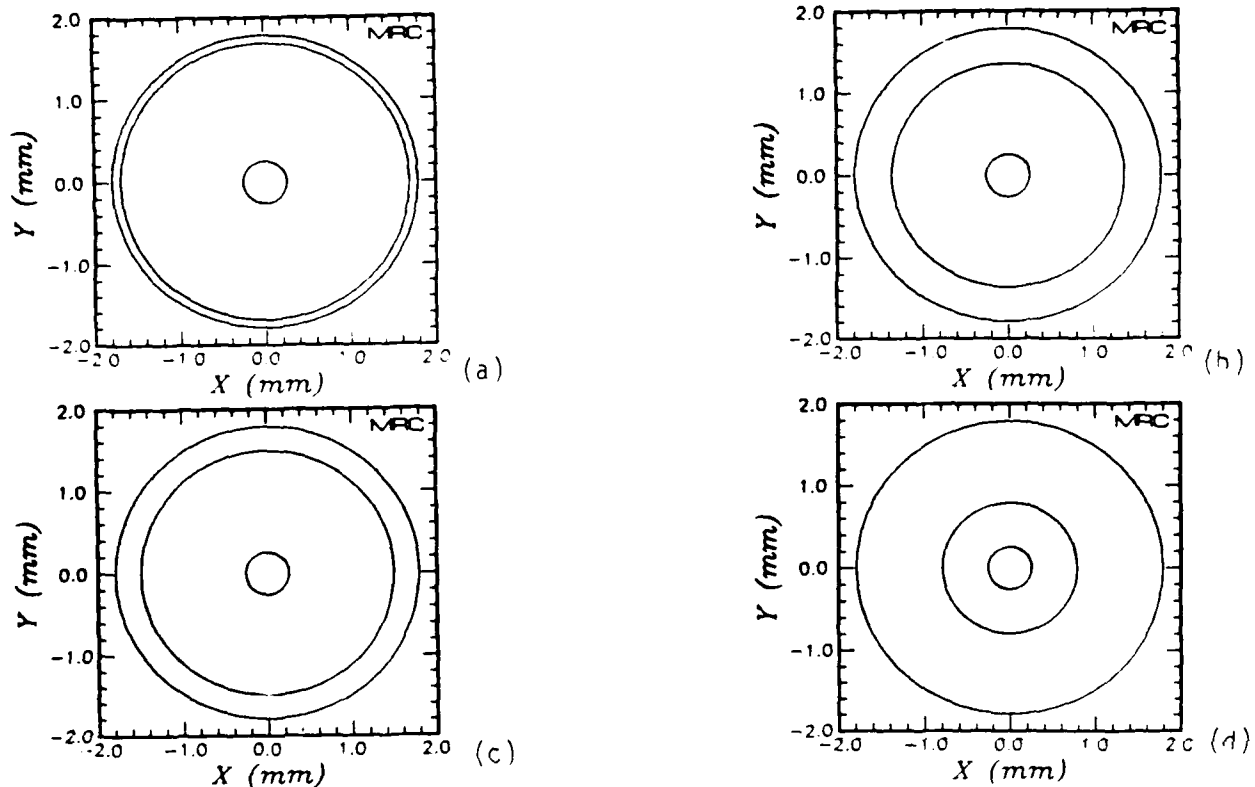
A series of parametric studies were conducted in order to understand the behavior of direct drive currents in coaxial cables. Based on these results a simple model was developed to estimate the currents generated from the shield and center conductors of a coaxial cable. Figure 3 shows the variation in the external currents induced by emission from the shield, dielectric and center conductors as a function of varying the diameter of the center conductor while holding the radius and thickness of the shield constant. One should note that not only does the center conductor increase its current contribution, but also, the shield contribution increases while that from dielectric material remains approximately constant. Although the center conductor increases its current contribution directly in relationship to its size as might be expected, one might not expect the shield current to increase in this case, since the shield thickness is held constant. However, the induced current on the center conductor, as pointed out earlier, is directly proportional to its image charge. The image charge is determined from the net potential difference an electron transverses in going from the shield towards the center conductor. Since the dielectric thickness decreases as the center conductor is increased, the gradient of the potential is increased. Therefore, an electron ejected from the shield traveling one mean free pathlength in the thin dielectric material will induce more charge on the center conductor than in the case of the thick dielectrical material.

Figure 4 shows the variation in the shield, dielectric and center conductor currents as a function of the shield thickness holding the outer radius of the shield R_s constant and letting the dielectric thickness vary. In the previous figure, we found the dielectric current to be of opposite sign and roughly the same magnitude of the center conductor current with the shield current dominating the net flow of current. In Figures 4a and 4d we explore this idea, first by reducing the shield thickness dramatically, and then, by radically increasing the



		Radius (mm)	J	J/JN
(a)	Shield	1.79	-1.13E-8	.61
	Dielectric	1.49	-1.11E-8	.60
	Conductor	.255	4.02E-9	-.22
	JN		-1.84E-8	
(b)	Shield	1.79	-1.55E-8	.67
	Dielectric	1.49	-1.36E-8	.59
	Conductor	.456	6.06E-9	-.26
	JN		-2.30E-8	
(c)	Shield	1.79	-4.56E-8	1.14
	Dielectric	1.49	-1.35E-8	.34
	Conductor	.957	1.91E-8	-.48
	JN		-4.00E-8	

Figure 3. The shield, dielectric, and center conductor "currents" (J in (coul/m)/(cal/cm²) as determined from the Monte Carlo code MCABLE and their ratio to the net current J_N as a function of size of the center conductor. The radius and thickness of the shield is held fixed. Figure a corresponds to cable UT141-75C and Figure b corresponds to cable UT141A. The shield and center conductors are made of copper and the dielectric material is teflon.



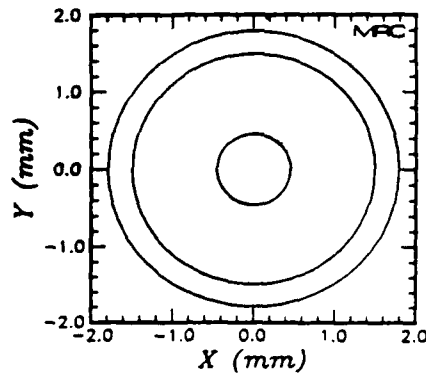
		<u>Radius</u>	<u>J</u>	<u>J/JN</u>
(a)	Shield	1.79	-5.92E-9	.43
	Dielectric	1.69	-1.00E-8	.72
	Conductor	.255	2.18E-9	-.16
	JN		<u>-1.38E-8</u>	
(b)	Shield	1.79	-1.13E-8	.61
	Dielectric	1.49	-1.11E-8	.60
	Conductor	.255	4.02E-9	-.22
	JN		<u>-1.84E-8</u>	
(c)	Shield	1.79	-1.49E-8	.78
	Dielectric	1.36	-8.24E-9	.43
	Conductor	.255	4.11E-9	-.22
	JN		<u>-1.90E-8</u>	
(d)	Shield	1.79	-1.79E-8	2.13
	Dielectric	.79	3.86E-10	-.05
	Conductor	.255	9.11E-9	-1.09
	JN		<u>-8.39E-9</u>	

Figure 4. The shield, dielectric, and center conductor "currents" J (coul/m)(cal/cm²) as determined from the Monte Carlo Code MCABLE and their ratio to the net current JN as a function of the shield thickness. The radii of the shield and the center conductors are held fixed.

thickness. In Figures 4a, b and c we see that it is very difficult to reduce the net current by reducing the thickness of the dominating shield current, while maintaining the same shield radius. In Figure 4d we have gone to the other extreme and increased the thickness, such that, the active area in the cable has been significantly reduced. This is not the same as just reducing the thickness of the dielectric material, since the response in Figure 3c is four times greater than Figure 4d with the same dielectric thickness and overall cable diameter.

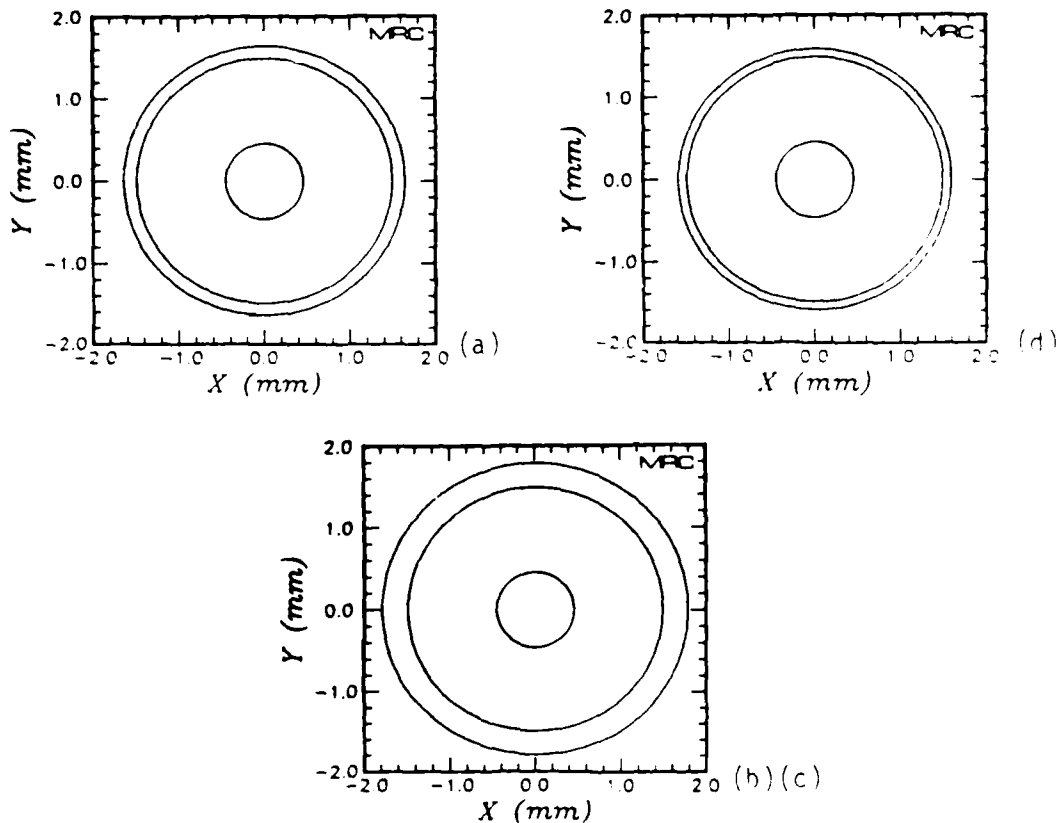
Since we are not restricted to dimensional variations, in Figure 5 we look at the effects on the individual and net currents produced by changing the material types within a cable and the radiating energy spectrum which drive these currents. In Figure 5a the effectiveness of a copper shielded cable is compared to that of an aluminum shielded cable in Figure 5b, which results in a 50% decrease in the net current. In Figures 5c and 5d the teflon dielectric is replaced with a polyethylene dielectric, and once again a 50% reduction in the net currents is achieved. Both of these reductions in net current are easily understood, since the interaction of gamma rays is highly dependent upon the density of the material being used. The densities of copper, aluminum, teflon and polyethylene are 8.96, 2.70, 2.20 and 0.92 gm/cm³ respectively. The last two parts of Figure 5, Figures 5e and 5f, along with Figure 5a, show a variation in the net current from $-2.45E-8$ (coul/m)/(cal/cm²) to $-2.09E-8$ (coul/m)/(cal/cm²) for 0.8 Mev and 1.3 Mev gamma rays respectively.

Although we have looked at dimensional, material, and energy variations, in Figure 6 we consider varying the shield thickness while holding the dielectric and center conductor dimensions fixed for two materially different cables. In these figures, we can see the direct response of current to variations in the shield thickness, while the dielectric and inner conductor currents remain approximately fixed. As shown in this figure and previous figures, the shield and/or dielectric



	<u>J</u>	<u>J/JN</u>	<u>Material</u>		<u>J</u>	<u>J/JN</u>	<u>Material</u>
(a) Shield	-1.55E-8	.67	Copper	(b) Shield	-2.07E-8	1.63	Copper
Dielectric	-1.36E-8	.59	Teflon	Dielectric	-5.89E-9	.46	Polyethylene
Conductor	6.06E-9	-.26	Copper	Conductor	8.97E-9	-.71	Copper
JN	-2.30E-8			JN	-1.27E-8		
(c) Shield	-8.50E-9	.73	Aluminum	(d) Shield	-8.26E-9	2.0	Aluminum
Dielectric	-6.96E-9	.59	Teflon	Dielectric	-2.80E-11	.01	Polyethylene
Conductor	3.78E-9	-.32	Copper	Conductor	4.32E-9	-1.01	Copper
JN	-1.17E-8			JN	-4.28E-9		
	<u>E_γ = 0.8 Mev</u>				<u>E_γ = 1.3 Mev</u>		
(e) Shield	-1.08E-8	.44	Copper	(f) Shield	-2.30E-8	1.10	Copper
Dielectric	-1.83E-8	.75	Teflon	Dielectric	-6.43E-9	.31	Teflon
Conductor	4.57E-9	-.19	Copper	Conductor	8.54E-9	-.41	Copper
JN	-2.45E-8			JN	-2.09E-8		

Figure 5. The shield, dielectric, and center conductor "currents" (coul/m)/(cal/cm²) as determined from the Monte Carlo code MCABLE and their ratio to the net current as a function of various material types as labeled in Figures a through d. In addition, the cable listed in Figure a was also used in Figures e and f but their responses were determined at gamma energies of 0.8 Mev and 1.3 Mev instead of 1.0 Mev. The dimensions are R_S = 1.79 mm, R_D = 1.49 mm and R_C = 0.456 mm and this cable corresponds to UT141A.

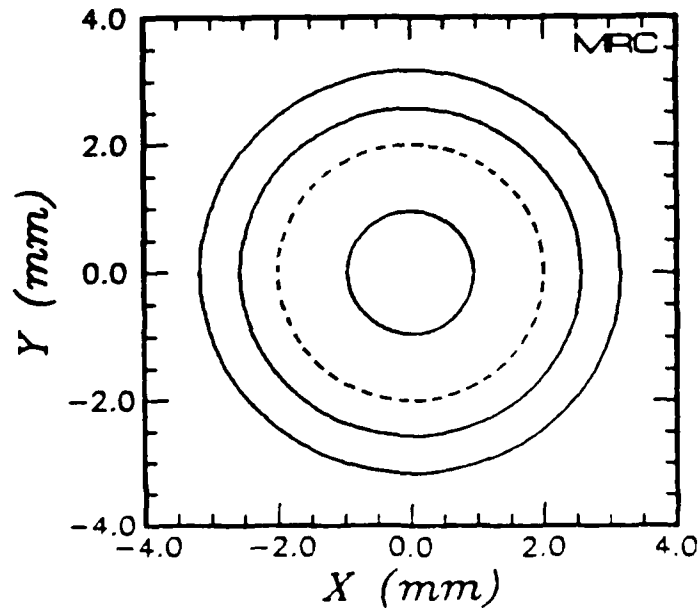


		Radius	J	J/JN	Material
(a)	Shield	1.64	-1.03E-8	.62	Copper
	Dielectric	1.49	-1.21E-8	.73	Teflon
	Conductor	.456	5.83E-9	-.35	Copper
	JN		-1.66E-8		
(b)	Shield	1.79	-1.55E-8	.67	Copper
	Dielectric	1.49	-1.36E-8	.59	Teflon
	Conductor	.456	6.06E-9	-.26	Copper
	JN		-2.30E-8		
(c)	Shield	1.79	-8.62E-9	2.01	Aluminum
	Dielectric	1.49	-2.80E-11	.01	Polyethylene
	Conductor	.456	4.31E-9	-1.01	Copper
	JN		-1.90E-8		
(d)	Shield	1.59	-2.43E-9	2.13	Aluminum
	Dielectric	1.49	-2.45E-9	2.15	Polyethylene
	Conductor	.456	3.73E-9	-3.27	Copper
	JN		-1.14E-9		

Figure 6. The shield, dielectric, and center conductor "currents" (coul/m)/(cal/cm²) as determined from the Monte Carlo code MCABLE and their ratio to the net current as a function of the shield thickness for two different sets of materials. The radius of the dielectric and the center conductor are fixed.

currents dominate the inner conductor current in a single conducting coaxial cable unless they are significantly less dense than the inner conductor material. However, in Figure 6d we did not achieve a reversal in the flow of net current even with a very thin aluminum shield and a polyethylene dielectric.

We still have not covered one very important aspect governing the response of cables due to gamma radiation, and that is, the air gap. The air gap in cables not only affects the material and geometrical aspects of a cable, but also, serves as a reservoir for storing charge which is released during gamma and X-ray radiation. In this report, we are only concerned with the material and geometrical aspects of air gaps within cables as shown in Figure 7. In Figures 7a and 7b, we notice that although the teflon and polyethylene currents are positive, we have not discovered anything new here. We have merely given the electrons created in these dielectric materials the opportunity to travel through a greater potential difference before being conducted away from the shield. The same phenomenon would be true if we sliced the teflon dielectric in Figure 7c in half. The outer teflon ring would yield a negative current and the inner ring a positive current with the same net current. Although we might be pleased by the fact that no net current was generated in the gap, we must also remember that the lower density of the air gap lets electrons travel a greater distance into the cable generating larger shield currents. This is seen by comparing the shield currents in Figures 7a, 7b and 7c. Figure 7a represents the Adams-Russell FN-30 cable which is constructed with an inner solid teflon ring around the center conductor followed by an outer perforated teflon ring. Figure 7b contains the approximate dimensions of the Andrew FHJ1-50 cable which used foamed polyethylene as its dielectric material. Figure 7c has no air gap and provides a comparison with the above two cables.



		<u>Radius</u>	<u>J</u>	<u>J/JN</u>	<u>Material</u>
(a)	Shield	3.16	-1.05E-7	1.33	Copper
	Air Gap	2.57	0.0	0.0	Air
	Dielectric	2.00	1.77E-8	-.22	Teflon
	Conductor	.953	7.84E-9	-.10	Copper
	JN		<u>-7.91E-8</u>		
(b)	Shield	3.16	-1.014E-7	1.79	Copper
	Air Gap	2.57	0.0	0.0	Air
	Dielectric	2.00	2.70E-8	-.48	Polyethylene
	Conductor	.953	1.78E-8	-.31	Copper
	JN		<u>-5.66E-8</u>		
(c)	Shield	3.16	-3.70E-8	.43	Copper
	Dielectric	2.57	-6.27E-8	.72	Teflon
	Conductor	.953	1.27E-8	-.15	Copper
	JN		<u>-8.70E-8</u>		

Figure 7. The shield, dielectric, and center conductor "currents" (coul/m)/(cal/cm²) as determined from the Monte Carlo code MCABLE and their ratio to the net current as a function of two different dielectric materials with and without an air gap. The density of teflon is 2.2 gm/cm³, polyethylene is 0.92 gm/cm³ and the radii dimensions are in millimeters. Figure a corresponds to cable FN-30 and Figure b is approximately cable FHJ1-50. Figure c shows the effect of removing the air gap in Figure a.

2.4 Aspects of Modeling

Based on this parametric study one cannot resist the temptation to put forth a simple model for predicting the induced currents in a cable due to gamma radiation. It would seem reasonable that given the emission currents for the shield and center conductor and the mean free path of an electron in all the materials involved, that one could write an expression for the induced currents from both the shield and center conductor. We know from elementary physics that the equipotential lines in a coaxial cable are given by the formula

$$V = \frac{V_1}{\ln(R_d/R_c)} \ln(R/R_c) \quad (14)$$

where R_d = radius of the dielectric material

R_c = radius of the center conductor

R = any arbitrary radius between R_c and R_d

and V_1 = the potential difference between the shield and center conductor. Since we are interested in fractions of electron charge which are induced on the conductors, we set V_1 equal to 1.0. As in our earlier discussion on validation checks, we showed that the currents recorded in the Monte Carlo code for a parallel plate capacitor are related to a material's emission current times the mean forward range of an electron. In a twisted cable this adds several complicating factors due to the geometry and the different materials of the cable. However, for a single conductor coaxial cable we would expect the random direction of gamma rays crossing the cable, simulating a twisted cable (see Figure 1), to give us the same response as a non-twisted cable due to its symmetry. This only simplifies our concept from randomly directed gamma rays crossing the

cable to a uniform pattern of gamma rays coming from one direction. We still must compute an effective range, instead of using the mean forward range for electrons emitted from either the shield or center conductor, due to the geometry and different materials involved in a cable. As in the previous analysis of emission currents where the induced current J was written in terms of the emission current J_E times the average potential difference $\overline{\Delta\phi}$ an electron transverses, the induced current in a cable can be determined from Equation 13 as

$$J(\text{coul/m})/(\text{cal/cm}^2) = J_E \overline{\Delta\phi} 200 R_s \quad (15)$$

The average potential difference in this case is determined from Equation 14 as

$$\overline{\Delta\phi}_s = \phi_r - \phi_d = \frac{1}{\ln(R_d/R_c)} \left(\ln \frac{R_d - R_\epsilon}{R_c} - \ln \frac{R_d}{R_c} \right) = \frac{1}{\ln(R_d/R_c)} \ln \frac{R_d - R_\epsilon}{R_d} \quad (16)$$

for an electron ejected from the shield and as

$$\overline{\Delta\phi}_c = \phi_r - \phi_c = \frac{1}{\ln(R_d/R_c)} \ln \frac{R_c + R_\epsilon}{R_c} \quad (17)$$

for an electron ejected from the center conductor

where R_d = radius of the dielectric material

R_c = radius of the center conductor

and R_ϵ = the effective range of an electron in transversing the equipotential lines of a cable.

Although the effective range R_{ϵ} for an electron emitted from either the shield or center conductor can be determined in MCABLE by single point emission from several positions on either conductor, let us estimate the value R_{ϵ} . The electrons which are emitted from gamma rays passing through the center of the cable will have a range equaled to a combination of the mean forward range in the conductor with that of the dielectric material. We will select the average value of these two ranges for our first order approximation. This average mean forward range of electrons entering the dielectric from the shield will continually be shorted by the curvature of the shield as the forward emission of electrons approaches a tangent to the dielectric material. We might expect the mean range to vary from a normalized value of 1.0 to 1/2 at the tangent, except the shield begins curving back and the electrons begin to make a transition from the upper half of the shield to the lower half. In addition, the average range of electron is not directed towards the center conductor but must be multiplied by a cosine term. Therefore, we have selected the effective range of a electron emitted from the shield as the average value of the cosine function between zero and 90 degrees squared times the average forward range of the two materials. This should also work to a first approximation for the center conductor since the mean free path of electrons in the center conductor approaches zero as the gamma rays approach a tangent to the center wire.

As in the previous parallel plate capacitor model, when using the emission current J_{ϵ} , we are assuming that a steady state flow of electrons exist across each interface and that the number of electrons generated per unit area is proportional to the number of gamma rays for the same unit area. Since a steady state flow of electrons requires that the material be at least four or five mean free electron paths thick, we can expect the effective diameter of the center conductor to be reduced

slightly. The area of the center conductor to the total area of radiation is proportional to R_c/R_s . Likewise, the area of the shield which is contributing induced current to the total area of radiation is proportional to R_d/R_s . Multiplying Equation 15 by each of these ratios gives us the following two equations for predicting the response of either the shield or center conductor.

$$J_s (\text{coul/M}) / (\text{cal/cm}^2) = J_E \overline{\Delta\phi_s} R_d / 200 \quad (18)$$

$$J_c (\text{coul/M}) / (\text{cal/cm}^2) = J_E \overline{\Delta\phi_c} R_c / 200 \quad (19)$$

where R_d = the radius of the dielectric material in centimeters

R_c = the radius of the center conductor in centimeters.

and R_E = .405 times the average mean forward range.

The predicted values J_p for the shield and center conductor currents are shown for Figures 3 and 4 in Table 3. One should note that although the average error factor, or ratio of the predicted value to the Monte Carlo result is large, the standard deviation is small except for Figure 4a. There are two separate reasons for the large deviation in Figure 4a. First, the shield is very thin, less than 2 mean free electron pathlengths thick which did not permit a steady state flow of electrons to be achieved, and secondly, there were insufficient statistics taken in recording the center conductor current. The average error factor for the shield is 1.75 and 3.75 for the center conductor. Although this model does not attempt to predict the values exactly, it can be used to provide some insight into the generation of shield and center conductor currents.

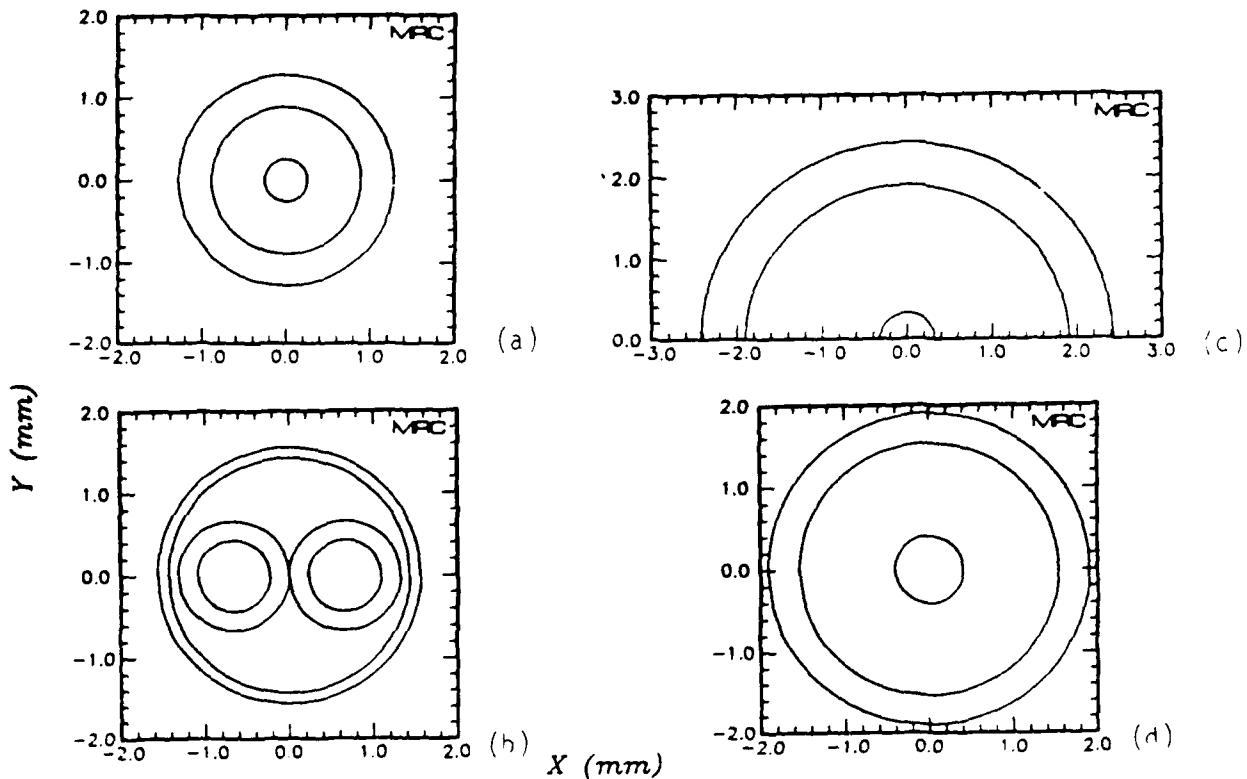
Table 3. The results of a simple analytical model are compared to those of the Monte Carlo code MCABLE.

Figure Number		Radius	J	JP	JP/J	JP/J
3a	Shield	1.79	-1.13E-8	-2.00E-8	1.77	3.95
	Dielectric	1.49				
	Conductor	.255	4.02E-9	1.59E-8		
3b	Shield	1.79	-1.55E-8	-2.98E-8	1.92	4.22
	Dielectric	1.49				
	Conductor	.456	6.06E-9	2.56E-8		
3c	Shield	1.79	-4.56E-8	-7.98E-8	1.75	3.79
	Dielectric	1.49				
	Conductor	.957	1.91E-8	7.24E-8		
4a	Shield	1.79	-5.92E-9	-1.86E-8	3.14	6.81
	Dielectric	1.69				
	Conductor	.255	2.18E-9	1.48E-8		
4c	Shield	1.79	-1.49E-8	-2.12E-8	1.42	4.08
	Dielectric	1.36				
	Conductor	.255	4.11E-9	1.68E-8		
4d	Shield	1.79	-1.79E-8	-3.24E-8	1.81	2.72
	Dielectric	.79				
	Conductor	.255	9.11E-9	2.48E-8		

2.5 Results

In Figure 8 we have computed the response of several cables that were tested⁸ in the Raytheon FX-25 Van der Graaf type flash X-ray machine. These cables, the two cables listed in Figure 7 and the UT141A cable in Figure 3 were exposed in air to a filtered spectrum using 1/4" of lead with an average gamma ray energy of slightly less than 1.1 Mev. Unless otherwise noted all of the Monte Carlo calculations were done at 1.0 Mev, since as shown in Figure 5 and confirmed by the test measurements, the induced currents are only weakly dependent upon energy in this region. Although the UT-101AL cable in Figure 8a is listed with both polyethylene and teflon, only the teflon version was tested and the polyethylene version is just being provided as a comparison. The MX cable in Figure 8b, which was referred to as Cable #1 in the Hi-Rel Laboratory report⁹, showed only slight changes in its response when radiated in a uniform fashion parallel and perpendicular to the center line of two conductor axes. The values listed in Figure 8b are for the twisted version of the MX cable. The last two cables are standard generic coaxial cables RG-59 and RG-58.

The Monte Carlo code calculations are compared to the measured values in Figure 9. Unfortunately, all of these measurements were performed in air with the exception of the Judd TSP cable, which was measured in a vacuum, and could be seriously effected by the release of stored charge within the cable. This is clearly demonstrated by the FN-30 cable which contained a perforated dielectric. The response is equal in magnitude to the predicted value by the Monte Carlo code MCABLE but of the opposite sign. Even in a vacuum, the response of this cable remained positive. The measured values for the UT-141A and MX cables were also effected by the release of stored charge, since the measured response of the UT-141A cable is less than the UT-101AL cable and the MX measurement is far below the Judd TSP measurement. We know from the physics of the



		Radius	J	J/JN	Material	J	J/JN	Material
(a)	Shield	1.28	-4.74E-9	2.69	Aluminum	-6.04E-9	1.36	Aluminum
	Dielectric	.890	5.71E-10	-.32	Polyethylene	-8.00E-10	.18	Teflon
	Conductor	.255	2.41E-9	-1.37	Copper	2.41E-9	-.54	Copper
	JN		-1.76E-9			-4.43E-9		
(b)	Shield	1.56	-1.81E-7	1.28	Copper			
	Filler	1.43	-8.19E-9	.58	New Filler			
	Dielectric	.66	3.68E-9	-.26	Raychem 55 (Tefzel)			
	Conductor	.43	8.53E-9	-.60	Copper			
JN		-1.41E-8						
(c)	Shield	2.43	-2.71E-8	1.06	Copper			
	Dielectric	1.91	-5.88E-9	.23	Polyethylene			
	Conductor	.321	7.39E-9	-.29	Copper			
	JN		-2.56E-8					
(d)	Shield	1.91	-2.38E-8	1.43	Copper			
	Dielectric	1.54	-1.43E-9	.09	Polyethylene			
	Conductor	.406	8.48E-9	-.51	Copper			
	JN		-1.67E-8					

Figure 8. The shield, dielectric, and center conductor "currents" (coul/m)/(cal/cm²) and their ratio to the net current for various cables tested. Figure a corresponds to cable UT-101AL. Figure b corresponds to the MX cable. Figures c and d are standard generic cables RG-59 and RG-58 respectively.

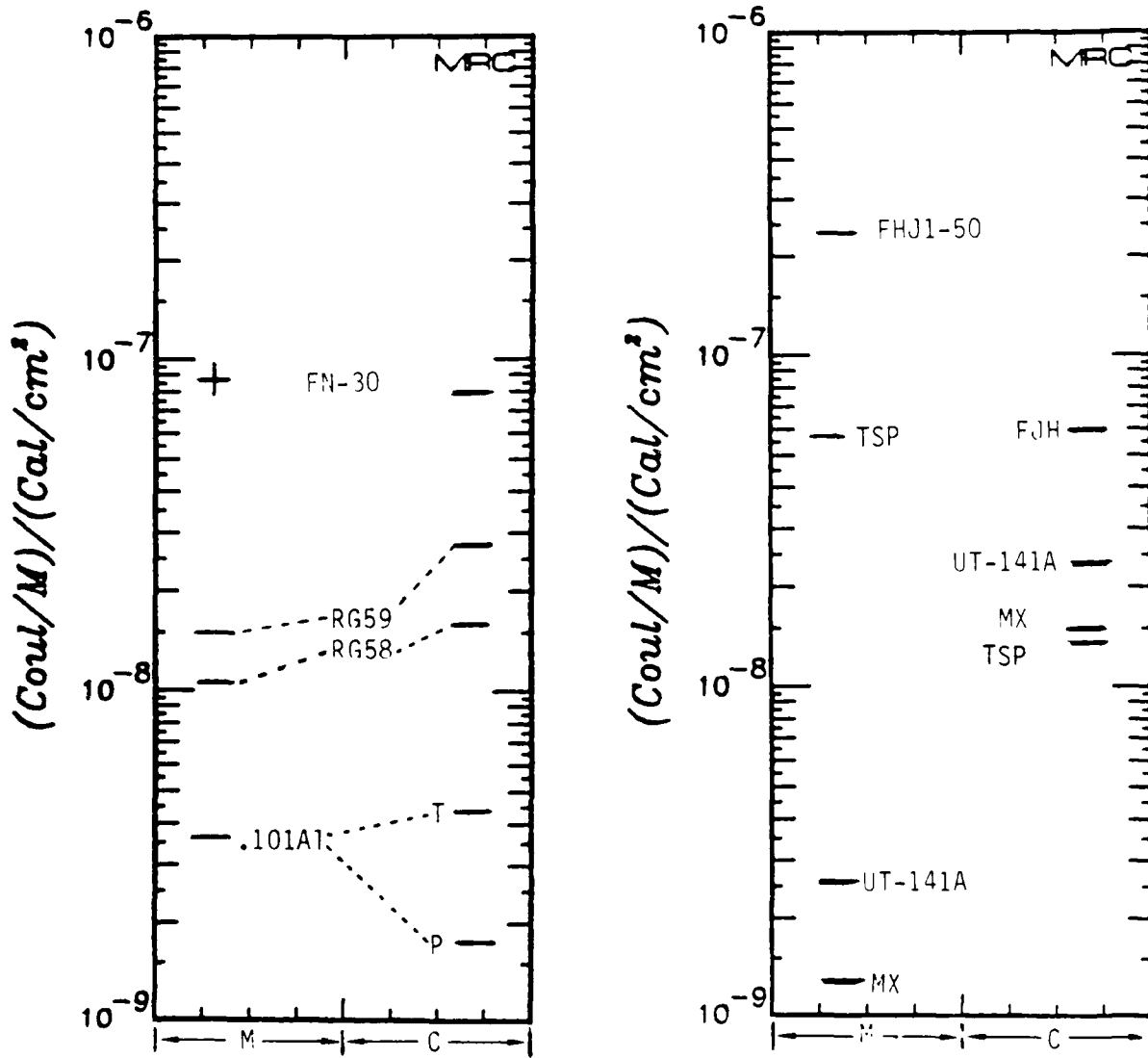


Figure 9. This is a comparison between the measured (M) and calculated (C) responses of 8 cables using the computer code MCABLE. All of the cables were tested in air with an average gamma energy of 1.0 Mev except the Judd TSP cable which was tested at 0.86 Mev in a vacuum. The calculated values for UT-101A1 cable were done for both teflon and polyethylene, although the cable was listed as containing teflon. The exact dimensions of FHJ1-50 were not obtained, however, FJH is believed to be a close approximation. All the measured and calculated values are negative with the exception of the measured value for FN30. It is positive.

situation as confirmed in Figures 5a and 5c that the aluminum shielding on the UT-101A1 cable will produce fewer electrons flowing into the inner conductor than the copper shield on the UT-141A cable. Therefore, we would expect, as confirmed by the calculated values, that the response of the UT-101A1 cable would be significantly less than that of the UT-141A cable. However, in the case of the MX and Judd TSP cables where the Judd cable is approximately 0.81 times the dimensions of the MX cable, we might expect the Judd TSP cable response to be about the same as the MX cable. The MX cable contained Raychem 55, which is another form of Tefzel, with a density of 1.7 and a filler labeled New Filler with a density of 1.17 gm/cm³. The Judd TSP cable contained polyvinyl chloride with a density of 1.7 gm/cm³. The calculated values are about the same but the measured values differ by a factor of 40. Although all of the measurements should have been performed in a vacuum to minimize the effects of stored charge, the agreement is still very good for the RG-58, RG-59 and UT-101A1 cables, as shown in Figure 9.

SECTION 3 CONCLUSIONS

The physical mechanics of determining the response of a cable due to gamma radiation is understood. An analytical model for both single and multi-conductor coaxial cables could be developed to aid in the design of low "gamma current" responding cables as demonstrated by the simple model proposed in this report and by the Monte Carlo Codes MCABLE and MCIMP. Although there are uncertainties in both measuring or modeling the dimensions, dielectric constants, densities and the chemical composition of a particular cable, the errors in these parameters are usually very small with respect to the error produced in determining the net current. Based on the parametric study conducted in this report, the problem of reliability predicting the response of a cable above 0.5 Mev is dependent upon the release of stored charge within the cable. Although no attempt has been made in this report to predict the amount of stored charge released from a cable due to gamma radiation, it can be orders of magnitude greater than the values predicted here. As demonstrated in the gamma ray direct drive measurements, the FN-30 cable's response in a vacuum fell to 8% of its air value.⁸ However, this cable was designed with a partially perforated dielectric and one might anticipate a large amount of stored charge. The measured value in air, as shown in Figure 9, is equal in magnitude to the predicted value but of the opposite sign.

The Monte Carlo codes MCABLE and MCIMP are designed to predict the direct drive currents due to gamma radiation above 200 Kev. Although the Moliere single and multiple scattering formulas are valid for kinetic energies of the scattered particle to be as low as 3 to 10 Kev, the Scott-Snyder approximations are made for nominal thicknesses of Ω_0 equaled

to 100 or more. We have found through the use of the MCIMP code in its range determinations given in Table 1 that 10 or more scatterings per pathlength are required to achieve results which are accurate and independent of the number of scatterings. This requires that the gamma radiation energy be at least 200 KeV. Since we were only concerned with gamma ray energies above 0.8 MeV in this report, we did not include a separate energy and angular distribution function for any of the created photoelectric electrons. We merely treated them as Compton electrons, since their contribution to the current is small for gamma ray energies above 0.25 MeV for low Z elements like aluminum and 0.6 MeV for copper.

The accuracy of the Monte Carlo codes was verified by the range and emission current determinations in Tables 1 and 2, and by the SPED experiment. The results from the MCIMP code and the Photo-Handbook for the mean value of electron ranges in different materials were in very good agreement. The forward and backward emission currents as calculated by the MCIMP code were low in comparison to the values from the QUICKE2 code. However, the calculated value from the MCIMP code of $-3.0E-9$ coul/cal for the SPED device, which was designed to provide an accurate measurement of emission currents, was slightly larger than the vacuum measurement of $-2.75E-9$ coul/cal. Conversely, the response of Judd TSP cable, which reversed sign when placed in a vacuum, was a factor of 4 greater than that predicted by MCABLE. Although the air measurements and the calculated values are in very good agreement for the RG-58, RG-59 and UT-101A1 cables, more vacuum measured data should be used to further establish the accuracy of the MCABLE and MCIMP codes and to resolve any small differences between these codes and the QUICKE2 code. The MCABLE and MCIMP codes can be used to predict the response of multi-conductor cables and any arbitrarily shaped device or cable.

LIST OF REFERENCES

1. Potter, David, Computational Physics, John Wiley & Sons, New York, N.Y., 1973.
2. Evans, Robley D., The Atomic Nucleus, McGraw-Hill Book Company, Inc. 1955.
3. Longmire, C. L. "Effect of Multiple Scattering on the Compton Recoil Current," Mission Research Corporation, DNA 4543T, (MRC-R-378), February 1978.
4. Dellin, T. A. and C. J. Mac Callum, A Handbook of Photo-Compton Current Data, Sandia Laboratories, SCL-RR-720086, December 1972.
5. Dellin, T. A. and C. J. Mac Callum, "QUICKE2: A One-Dimensional Code for Calculating Bulk and Vacuum Emitted Photo-Compton Currents," Sandia Laboratories, SLL-74-0218, April 1974.
6. Chadsey, W. L. and C. W. Wilson, "X-Ray Photoemission," Science Applications, Incorporated, SAI-75-558-WA, June 1975.
7. Savage, E. B., "Notes on the Meca X-ray Tests," Mission Research Corporation, April 1984.
8. Chervenak, J. G., "Gamma-Ray Direct Drive of the Sentry Sec Candidate Cables/Connectors using a FX-25," Mission Research Corporation, MRC/SD-R-126.
9. Hi-Rel Laboratories, "Photodocumentation," Mission Research Corporation MR-121115 January 4, 1982.
10. Scott, William T., "The Theory of Small-Angle Multiple Fast-Scattering of Charged Particles," Review of Modern Physics, Vol 35, 231, April 1963.
11. Ziock, Klaus, Basic Quantum Mechanics, John Wiley & Sons, Inc. New York, N.Y., 1969.
12. Morse and H. Fishback, Methods of Theoretical Physics, McGraw-Hill Book Company, Inc. New York, 1953.

13. Fleischmann, H. Z., "Zur Kleinwinkeltheorie der Vielfachstreuung", Naturforsch, Vol 15a, 1090, 1960.
14. Bethe, Physical Review, Vol 89, 1256, 1953.
15. Scott, W. T., "Mean-Value Calculations for Projected Multiple Scattering," Physical Review, Vol 85, 245, 1952.
16. C. L. Longmire, "Considerations in SGEMP Simulation", SSN-194, Mission Research Corporation, May 1974.

APPENDIX SINGLE AND MULTIPLE SCATTERING THEORY

Multiple scattering of charge particles by atoms first became relevant to particle physics with Rutherford's discovery of the nucleus by means of scattering alpha particles by thin foils. The following discussion will provide a brief synopsis of the development of single and multiple scattering theory from this 1911 experiment in classical physics to the quantum mechanical solution obtained by Moliere. Finally, we will conclude with the Snyder-Scott solution due to its simplistic form and its agreement with Moliere's results. This discussion is not intended to be a rigorous mathematical derivation but merely to provide an overall view. (The reader interested in pursuing this subject should refer to the references for a more detailed mathematical explanation of the results presented here.)

Based on Classical Physics Rutherford's cross section of scattering was developed to explain the scattering of a charge particle from a bare nucleus of infinite mass. That is, Rutherford assumed that the only force between the alpha particle and the nucleus was an electrostatic $1/r^2$ force and that only the alpha particles direction of momentum would change while the nucleus remained stationary. Therefore, for a fast non-relativistic particle of charge ze which can easily penetrate the electron cloud surrounding a massive nucleus of charge Ze the Rutherford cross section will adequately describe the scattering of these particles. The Rutherford cross section¹⁰ is given by

$$\sigma_{Ru}(\theta) = \frac{(2ze^2/mv^2)^2}{(2\sin(\theta/2))^4} \quad (A-1)$$

where $1/2 mv^2$ is the kinetic energy of the particle. In the relativistic case, particles involving small angles are scattered according to the relativistic Rutherford cross section

$$\sigma_{Ru}(\theta) = \frac{4\alpha^2}{k^2\theta^4} \quad (A-2)$$

where the Born parameter α is given by

$$\alpha = \frac{zZ}{137\beta} = \frac{zZe^2}{\hbar v} \quad (A-3)$$

and the reciprocal of the wavenumber

$$\frac{1}{k} = \lambda_0 = \hbar/p \quad (A-4)$$

For our less energetic electrons this law must be modified to take in account the effects of screening and scattering by the atomic electrons, and the finite size and recoil effects of the scattering material. We must make a transition here from classical physics with its billiard ball analogies to quantum mechanics with its scattering wave analysis. In 1926 Erwin Schroedinger postulated that the classical equation of motion

$$E = \frac{p^2}{2m} + V(r) \quad (A-5)$$

could be replaced by the quantum mechanical wave equation

$$i\hbar \frac{\partial \psi}{\partial t} = -\frac{\hbar^2}{2m} \nabla^2 \psi + V(r)\psi \quad (A-6)$$

The time independent form of this equation can be found by applying the method of separation of variables with a separation constant E as

$$E\psi = -\frac{\hbar^2}{2m} \nabla^2 \psi + V(r)\psi \quad (\text{A-7})$$

where Ψ was replaced with $\psi(t)$. ψ represents our total wave function which can be decomposed into an incident wave or parallel beam of particles represented by a plane wave $\psi_i = e^{ikr}$ plus a scattered wave or particle beam propagating spherical outward by $\psi_s = f(\theta) e^{ikr} / r$, where $f(\theta)$ is called the scattering amplitude or angle-distribution factor. We can once again apply our separation of variables technique to the Schrodinger time independent equation if the nuclear potential function is spherically symmetric and the scattering region is isotropic. In polar coordinates this yields

$$\frac{d^2}{dr^2} + \left\{ k^2 - \frac{\ell(\ell+1)}{r^2} - \frac{2mV(r)}{\hbar^2} \right\} r\psi_\ell(r) = 0 \quad (\text{A-8})$$

and

$$\frac{1}{\sin\theta} \frac{\partial}{\partial\theta} \left(\sin\theta \frac{\partial\psi_\ell(\theta)}{\partial\theta} \right) = -\ell(\ell+1) \psi_\ell(\theta) \quad (\text{A-9})$$

where $\ell(\ell+1)$ is the separation constant. It is well known to students of quantum mechanics that the solutions to these two differential equations are given by a complete sum of Bessel functions for the radial equation and the Legendre polynomials for the θ equation.¹¹ Since we have assumed an isotropic medium without the presence of electrical or magnetic fields, and therefore, independent of ϕ , we can write the solution to Schrodinger's equation in the presence of a scattering potential as

$$\psi = \sum_{\ell=0}^{\infty} (a_\ell J_{\ell+1/2} + b_\ell J_{-\ell-1/2}) \frac{1}{\sqrt{kr}} P_\ell(\cos\theta) \quad (\text{A-10})$$

In the asymptotic case, that is, where our observation point is far from the atomic region of scattering, we can approximate the Bessel functions as follows:

$$J_{\ell+1/2} \underset{kr \rightarrow \infty}{\sim} \sqrt{\frac{2}{\pi kr}} \sin\left(kr - \frac{\ell\pi}{2}\right) \quad \text{for } \ell=0,1,2, \dots$$

$$J_{-\ell-1/2} \underset{kr \rightarrow \infty}{\sim} (-1)^\ell \sqrt{\frac{2}{\pi kr}} \cos\left(kr - \frac{\ell\pi}{2}\right) \quad \text{for } \ell=0,1,2, \dots$$

Furthermore, with the aid of a trigonometric identity we can write the solution for the ℓ^{th} partial wave as

$$\psi_\ell = \sqrt{\frac{2}{\pi}} \frac{1}{kr} C_\ell \sin\left(kr - \frac{\pi\ell}{2} + \delta_\ell\right) P_\ell(\cos\theta) \quad (\text{A-11})$$

$$\text{where } \tan \delta_\ell = \frac{(-1)^\ell b_\ell}{a_\ell} \quad (\text{A-12})$$

We can now equate our total wave function with the Schroedinger solution and solve for the scattered amplitude function. That is,

$$A \left\{ e^{ikz} + f(\theta) \frac{e^{-ikr}}{r} \right\} = \sqrt{\frac{2}{\pi}} \frac{1}{kr} \sum_{\ell=0}^{\infty} C_\ell \sin\left(kr - \frac{\pi\ell}{2} + \delta_\ell\right) P_\ell(\cos\theta) \quad (\text{A-13})$$

In the absence of a scattering potential

$$A e^{ikz} = \sqrt{\frac{2}{\pi}} \frac{1}{kr} \sum_{\ell=0}^{\infty} C_\ell a_\ell \sin\left(kr - \frac{\pi\ell}{2} + \delta_\ell\right) P_\ell(\cos\theta) \quad (\text{A-14})$$

Therefore, if we write the sine functions in terms of their exponentials e^{ikr} and e^{-ikr} , which are linearly independent, we can equate their coefficients and solve for $f(\theta)$.

$$f(\theta) = \sqrt{\frac{2}{\pi}} \frac{1}{2ikA} \sum_{\ell=0}^{\infty} a_{\ell} e^{-\pi\ell/2} (e^{2i\delta_{\ell-1}}) P_{\ell}(\cos\theta) \quad (\text{A-15})$$

We can proceed one step further by taking advantage of the orthogonality properties of the Legendre polynomials and solve for the constants a_{ℓ} by multiplying Equation 14 by $P_n(\cos\theta)$ and integrating.

$$A \int_{-1}^1 P_n(\cos\theta) e^{ikr \cos\theta} d\cos\theta = \sqrt{\frac{2}{\pi}} \frac{1}{kr} \sum_{\ell} a_{\ell} \sin(kr - \frac{\pi\ell}{2}) \int_{-1}^1 P_{\ell}(\cos\theta) P_n(\cos\theta) d\cos\theta \quad (\text{A-16})$$

$$\text{where } \int_{-1}^1 P_{\ell}(\cos\theta) P_n(\cos\theta) d\cos\theta = \frac{2}{2\ell+1} \delta_{n\ell} .$$

The left hand side of Equation 16 can be simplified by partial integration as

$$A \int_{-1}^1 e^{ikr \cos\theta} P_{\ell}(\cos\theta) d\cos\theta = \frac{A}{ikr} e^{ikr} P_{\ell}(\cos\theta) \Big|_{-1}^1 - \frac{A}{ikr} \int_{-1}^1 e^{ikr \cos\theta} P_{\ell}^1(\cos\theta) d\cos\theta \quad (\text{A-17})$$

Since the second term on the right hand side of this equation is on the order of $1/r^2$, we can approximate the integral with the first term as

$$\frac{2 A i^{\ell}}{kr} \sin(kr - \frac{\pi\ell}{2})$$

Substituting this back into Equation 16 we get

$$a_{\ell} = Ai^{\ell} \sqrt{\frac{\pi}{2}} (2\ell+1) \quad (\text{A-18})$$

The solution for the scattering amplitude becomes

$$f(\theta) = \sum_{\ell=0}^{\infty} \frac{2\ell+1}{2ik} (e^{2i\delta_{\ell}} - 1) P_{\ell}(\cos\theta) \quad (\text{A-19})$$

The differential scattering cross section is given by the square of $f(\theta)$ as

$$\sigma(\theta) = \frac{1}{4k^2} \left| \sum_{\ell} (2\ell+1) (e^{2i\delta_{\ell}} - 1) P_{\ell}(\cos\theta) \right|^2 \quad (\text{A-20})$$

and the phase factor¹² is given by

$$\sin \delta_{\ell} = -\frac{2m}{\hbar^2} \int_0^{\infty} r dr \left(\frac{\pi kr}{2}\right)^{1/2} J_{\ell+1/2}(kr) V(r) \psi_{\ell}(r) \quad (\text{A-21})$$

This differential scattering cross section $\sigma(\theta)$ represents an asymptotic solution to Schroedinger's equation for the elastic scattering of particles incident from an arbitrary but spherically symmetric nuclear potential barrier $V(r)$. Before we apply this solution to Moliere's complicated potential function, let us first look at a simple function. One of the simplest models of electronic screening of the nucleus is called the Yukawa potential which is represented by a single exponential factor.

$$V(r) = \pm z \frac{Ze^2}{r} e^{-\mu r/r_0}$$

where r_0 is the Thomas-Fermi radius

$$r_0 = 0.468 \cdot 10^{-8} Z^{1/3} \text{ cm}$$

and μ is an arbitrary factor of the order of unity. The first Born approximation to the solution for the cross section is obtained by replacing $e^{2i\delta_\ell} - 1$ in Equation 20 by $2i\delta_\ell$ and $\psi_\ell(r)$ in the phase factor equation with the Bessel function solution to Equation 8 with $V(r)=0$

$$\delta_\ell = -\frac{\pi m}{\hbar^2} \int_0^\infty r dr J_{\ell+1/2}^2(kr) V(r) \quad (\text{A-23})$$

This yields a cross section of

$$\sigma(\theta) = \frac{4\alpha^2}{k^2 [2 \sin^2(\frac{\theta}{2}) + \mu^2/k^2 r_0^2]^2} \approx \frac{4\alpha^2}{k^2(\theta^2 + x_\mu^2)^2} \quad (\text{A-24})$$

where the Born screening angle x_μ is given by

$$x_\mu = \mu x_0 = \frac{\mu}{kr_0} = \frac{\mu \hbar}{pr_0} = \mu \frac{\lambda_0}{r_0} \quad (\text{A-25})$$

and $x_0 = \frac{1.13}{137} Z^{1/3} (m_e c/P)$ radians (A-26)

We can write this result in the form of Rutherford's formula with a screening factor $q(\theta)$ as

$$\sigma(\theta) = \frac{4\alpha^2}{k^2 \theta^4} q(\theta) \quad (\text{A-27})$$

where $q(\theta) = \frac{\theta^4}{(\theta^2 + x_\mu^2)^2}$ (A-28)

Let us put this screening factor into its proper perspective. Since the screening factor approaches 1.0 for large angles of scattering, it will have no effect on determining the scattering cross section. However, for small angles of scattering the screening factor will be very effective since $q(\theta)$ approaches zero. This means that a particle passing far from the nucleus will be perturbed by the electron cloud and undergo a small deflection. Even for the largest values of Z (the biggest electron clouds) a 210 Kev electron, which corresponds to an electron rest mass momentum of 1.0 ($p \approx m_e c$), will have a Born screening angle of only 2 degrees (see Equation 26). Although one may be tempted to ignore this small deflection, a later solution will show us that to a first order approximation $f(\theta)$ has a Gaussian distribution with the majority of scatterings occurring at small angles. In addition, we will find that the Moliere screening angle is larger due to an additional energy depend term α^2 as defined in Equation 3.

Moliere attempted to extend the first Born approximation which is valid for $\alpha \ll 1$, to a formula valid for lower energies (3 Kev) and angles up to 90° and to improve the exponential Yukawa screening potential by fitting the Thomas-Fermi function for heavy atoms with the sum of three exponentials. Let us recall two important approximations we made in the first Born approximation. First, the phase shift factor was found by using the incident unperturbed wave function $\psi_i(r)$ in Equation 21 rather than the scattered wave function due to its dependency on δ_ℓ . Moliere improves his solution by replacing the $k^2 - 2mV(r)/\hbar^2$ in Equation 8 with the relativistic value k_r^2 and rewrites the Schroedinger equation in its relativistic form as:

$$\left[\frac{d}{dr^2} + \frac{1}{r} \frac{d}{dr} - \frac{(\ell + 1/2)^2}{r^2} + k_r^2(r) \right] r^{1/2} \psi_\ell(r) = 0 \quad (\text{A-29})$$

where $k_r(r) = \frac{1}{\hbar c} \{ (E - V(r))^2 - m^2 c^4 \}^{1/2} \quad (\text{A-30})$

Assuming the asymptotic form of $\psi_\ell(r)$ to contain a phase factor $e^{i\gamma_\ell}$ he finds by the WKB method

$$\gamma_\ell(r) = -\frac{\pi}{4} + \int_{r_0}^r dr' \left[k_r^2(r') - \left(\frac{\ell + 1/2}{r'} \right)^2 \right]^{1/2} \quad (\text{A-31})$$

For the unscattered wave he replaces $k_r(r)$ with k and finds

$$\gamma_\ell^0(r) = -\frac{\pi}{4} + \int_{\rho}^r dr' \left[k^2 - \left(\frac{\ell + 1/2}{r'} \right)^2 \right]^{1/2} \quad (\text{A-32})$$

where $\rho = \frac{\ell + 1/2}{k}$

The phase shift δ_ℓ is then given by

$$\delta_\ell = \lim_{r \rightarrow \infty} [\gamma_\ell(r) - \gamma_\ell^0(r)] \quad (\text{A-33})$$

and if k_r^2 is expanded in powers of $V(r)/\hbar k v$ we find

$$\delta_\ell = \frac{\Phi(\rho)}{2} = -\frac{1}{\hbar v \rho} \int_{\rho}^{\infty} \frac{V(r) r dr}{(r^2 - \rho^2)^{1/2}} \quad (\text{A-34})$$

The other Born approximation involved replacing $e^{2i\delta_\ell} - 1$ in Equation 20 with $2i\delta_\ell$. Moliere improves his solution by replacing the summation in Equation 20 with an integral over a Bessel function which he then evaluated in various regions of energy (α) and angle (θ). This enables Moliere to avoid replacing $e^{2i\delta_\ell} - 1$ for large α . First Moliere replaces the Legendre Polynomials with the asymptotic formula for $P_\ell(\cos\theta)$

$$P_{\ell}(\cos\theta) \approx \left(\frac{\theta}{\sin\theta}\right)^{1/2} J_{\ell}[(\ell + 1/2)\theta] \quad (\text{A-35})$$

Then using Euler sum formula

$$\sum_{\ell=0}^{\infty} f(\ell + 1/2) = k \int_0^{\infty} f(k\rho) d\rho + \frac{1}{24} f'(0) + \dots$$

Moliere obtains a cross section of

$$\sigma(\theta) = k^2 \left(\frac{\theta}{\sin\theta}\right) \left| \int_0^{\infty} \rho d\rho J_0(k\theta\rho)(e^{i\phi(\rho)} - 1) \right|^2 \quad (\text{A-36})$$

However, Moliere observed that for small α and at large angles compared to the screening angle, the cross section should be proportional to θ^{-4} as in the small angle Rutherford scattering formula. Rewriting the Moliere cross section as

$$\sigma(\theta) = \frac{4\alpha^2(k\theta)^4}{4\alpha^2 k^2 \theta^3 \sin\theta} \left| \int_0^{\infty} \rho d\rho J_0(k\theta\rho)(e^{i\phi(\rho)} - 1) \right|^2 \quad (\text{A-37})$$

Moliere noted that $(\theta^3 \sin\theta)^{-1}$ agrees with the exact Rutherford formula within 0.5% up to 60 degrees. Therefore, in order to obtain a result that agrees with Rutherford results up to 90° and beyond Moliere replaced $(\theta^3 \sin\theta)^{-1}$ with $(2 \sin \theta/2)$. The Moliere cross section becomes

$$\boxed{\sigma_m(\theta) = \frac{4\alpha^2}{k^2 (2 \sin \theta/2)^4} q_m(\theta)} \quad (\text{A-38})$$

where the screening factor q_m is given by

$$q_m(\theta) = \frac{(k\theta)^4}{4\alpha^2} \left| \int_0^\infty \rho d\rho J_0(k\theta\rho) [e^{i\phi(\rho)} - 1] \right|^2 \quad (\text{A-39})$$

Equations 34, 38 and 39 represents Moliere's improved solution to the Schroedinger wave equation over the first Born approximation. Moliere made a further improvement in the nuclear potential barrier by fitting the Thomas-Fermi function for heavy atoms with a sum of three exponentials. Moliere's fit is given by

$$\omega_m(r') = 0.10e^{-6r'} + 0.55e^{-1.2r'} + 0.35e^{-0.3r'} \quad (\text{A-40})$$

where $r' = r/r_0$.

According to Moliere, this expression fits the exact Thomas-Fermi function within 0.2% for $0 < r' < 6$. The complete Moliere function is given by

$$V_m(r) = \pm \frac{zZe^2}{r} \omega_m(r') \quad (\text{A-41})$$

Substituting the potential function into Equation 34 and the phase shift function into Equation 39 Moliere finds a solution for $q(\theta)$ in three different regions of α and θ . Using the following definition for the Moliere screening angle χ_m

$$\ln \chi_m = -\frac{1}{2} - \lim_{\chi \rightarrow \infty} \left\{ \int_0^\chi d\theta \frac{q(\theta)}{\theta} - \ln \chi \right\} \quad (\text{A-42})$$

Moliere then solves for the screening angle χ_m in each of these regions and assuming a linear relationship between χ_m^2 and α^2 , Moliere writes a general expression for the screening angle over all regions of α and θ as

$$\boxed{\chi_m^2 = \chi_0^2 (1.13 + 3.76\alpha^2)} \quad (\text{A-43})$$

This enabled Moliere to propose a simple function for the screening factor $q(\theta)$, namely

$$\boxed{q_m(\theta) = \frac{\theta^4}{(\theta^2 + \chi_m^2)^2}} \quad (\text{A-44})$$

However, Fleischmann¹³ has suggested a better fit, especially for large α as

$$q(\theta) = \frac{\theta}{\theta + \chi_F} \quad (\text{A-45})$$

where $\chi_F = \chi_m e^{1/2}$

Using Equation 38, we can now write the Moliere single scattering probability function $W(\theta,t)$ as

$$W(\theta,t) = N(t) \sigma_m(\theta) \quad (\text{A-46})$$

where $N(t)$ = the number of independent scattering atoms per unit volume and $\sigma_m(\theta)$ is the Moliere differential cross section. Assuming azimuthal symmetry and small angle scattering, the probability of one scattering event occurring in a thickness dt at t through an angle between θ and $\theta+d\theta$ is given by

$$2\pi \theta d\theta W(\theta,t) dt = 2\pi \theta d\theta N(t) \sigma(\theta,t) dt$$

In the next section, we will use this single scattering function to determine the multiple scattering distribution function.

Multiple Scattering Theory

In this section, we will follow Scott's 1963 paper¹⁰ in discussing the basic ingredients into multiple scattering theory, the Moliere derivation, and the results presented by Snyder and Scott in that paper. Starting with the single scattering function, we will apply it to two or more successive scattering events in order to establish a probability or distribution function for the resulting scattered particles. In plane geometry we can write the probabilities of two single scatterings events between angles ϕ and $d\phi$ as $F_{1p}(\phi_1, t) d\phi_1$, and $F_{2p}(\phi_2, t) d\phi_2$, where each scattering function has been normalized.

$$\text{as } \int_{-\infty}^{\infty} F_{ip}(\phi_i, t) d\phi_i = 1$$

We know by ordinary rules of probability the resulting overall deflection ϕ due to these two successive scattering events would be given by

$$F_p(\phi, t) d\phi = d\phi \int_{-\infty}^{\infty} d\phi_1 F_{1p}(\phi_1, t) F_{2p}(\phi - \phi_1, t) \quad (\text{A-47})$$

where $\phi = \phi_1 + \phi_2$. This equation is more readily evaluated in "frequency" space by taking the Fourier transform of both sides. This yields

$$\tilde{F}_p(\xi, t) = \int_{-\infty}^{\infty} d\phi e^{i\xi\phi} \int_{-\infty}^{\infty} d\phi_1 F_{1p}(\phi_1, t) F_{2p}(\phi - \phi_1, t) \quad (\text{A-48})$$

$$\tilde{F}_p(\xi, t) = \int_{-\infty}^{\infty} d\phi_2 \int_{-\infty}^{\infty} d\phi_1 e^{i\xi(\phi_1 + \phi_2)} F_{1p}(\phi_1, t) F_{2p}(\phi_2, t) \quad (\text{A-49})$$

$$\tilde{F}_p(\xi, t) = \tilde{F}_{1p}(\xi, t) \tilde{F}_{2p}(\xi, t) \quad (A-50)$$

In polar coordinates the spatial angle distribution can be determined by converting the two dimensional Cartesian coordinate form of the Fourier transform into polar coordinates. In terms of the two projected angles ϕ_x and ϕ_y the Fourier transform is

$$\tilde{F}(\xi_x, \xi_y, t) = \int_{-\infty}^{\infty} d\phi_x \int_{-\infty}^{\infty} d\phi_y e^{i\xi_x \phi_x + i\xi_y \phi_y} F(\phi_x, \phi_y, t) \quad (A-51)$$

where in polar coordinates $\xi = (\xi_x^2 + \xi_y^2)$

$$\alpha = \tan^{-1} \frac{\xi_y}{\xi_x}$$

$$\xi_x = \xi \cos \alpha$$

$$\xi_y = \xi \sin \alpha$$

$$\phi_x = \tan \theta \cos \beta \approx \theta \cos \beta$$

and

$$\phi_y = \tan \theta \sin \beta \approx \theta \sin \beta$$

Substituting in the polar variables θ , β into Equation 51 we get

$$\tilde{F}(\xi, \alpha, t) = \int_0^{\infty} \theta d\theta \int_0^{2\pi} d\beta e^{i\xi\theta \cos(\beta-\alpha)} F(\theta, \beta, t) \quad (A-52)$$

If the normalized scattering distribution function is independent of azimuthal variations, the two dimensional transform reduces to a single Hankel transform

$$\tilde{F}(\xi, t) = 2\pi \int_0^{\infty} \theta d\theta J_0(\xi\theta) F(\theta, t) \quad (A-53)$$

where $J_0(\xi\theta)$ is the zero order Bessel function of the first kind and is given by

$$J_0(\xi\theta) = \frac{1}{2\pi} \int_0^{2\pi} d\beta e^{i\xi\theta \cos(\beta-\alpha)}$$

where the value of α is arbitrary. The inverse of this Hankel transformation is given by

$$F(\theta, t) = \frac{1}{2\pi} \int_0^\infty \xi d\xi J_0(\xi\theta) \tilde{F}(\xi, t) \quad (\text{A-54})$$

As in the plane geometry case, we can write the probability of an overall deflection in polar coordinates for each interval of $d\theta_i$ at θ_i and scattering positions t_i to t_i+dt_i as the product of each individual scattering event.

$$W(\theta_1)\theta_1 d\theta_1 d\beta_1 dt_1 W(\theta_2)\theta_2 d\theta_2 d\beta_2 dt_2 \dots \quad (\text{A-55})$$

Allowing for the probability of no scattering occurring within the interval $\Delta t = t - \sum_{i=1}^n dt$ and a homogenous substance with all W 's equal, one might expect to take the inverse of the n^{th} power of the Hankel transformation of the single scattering function $W(\theta)$ to achieve the correct result. However, if we wish to take into account all permutations of scatterings in the t_i intervals instead of successive scattering, we must multiply the transform function by $t^n/n!$. In equation form the Hankel transformation of the scattering function is

$$\omega(\xi) = 2\pi \int_0^\infty \theta d\theta J_0(\xi\theta) W(\theta) \quad (\text{A-56})$$

where θ is the single-scattering angle. The probability of no scatterings

occurring in an interval Δt is equaled to $e^{-\omega_0 \Delta t}$ where ω_0 is the reciprocal of the mean free pathlength. Combining the above terms, we get for the transform of the distribution function

$$\tilde{F}_n(\xi, t) = e^{-\omega_0 t} [\omega(\xi)t]^n / n! \quad (A-57)$$

where in the limit of the integrals Δt becomes t . The complete distribution in θ is determined from the sum of all scattering as

$$\tilde{F}(\xi, t) = \sum_{n=0}^{\infty} \tilde{F}_n(\xi, t) = e^{\omega(\xi)t - \omega_0 t} \quad (A-58)$$

Since in the Monte Carlo code we will select a scattering thickness over which the energy of the particle remains approximately constant, let us write the distribution function in terms of

$$\tilde{F}(\xi, t) = e^{[\Omega(\xi, t) - \Omega_0(t)]} \quad (A-59)$$

where $\Omega(\xi, t) = \int_0^t \omega(\xi, t') dt' = 2\pi \int_0^\infty \theta d\theta \int_0^t dt' J_0(\xi\theta) W(\theta, t')$

and $\Omega_0(t) = \int_0^t \omega_0(0, t') dt' = 2\pi \int_0^\infty \theta d\theta \int_0^t dt' W(\theta, t')$

The inverse of this function yields the spatial distribution function which is only dependent upon the single scattering function $W(\theta, t)$. Incidentally, we could have also achieved this same result from the Boltzman transport equation.¹⁰

Using the result from multiple scattering theory (Equation 59) and Moliere's cross section (Equation 38) let us solve for the spatial distribution function. From Equations 38 and 46, we can write the single scattering function in terms of Moliere's cross section as

$$W(\theta, t) = \frac{4 N(t) \alpha^2}{k^2 \theta^4} q_m(\theta) \quad (\text{A-60})$$

As in the multiple scattering formula, we wish to consider some nominal thickness or scattering length t over which the energy of the particle does not vary much. In a non-homogenous material or at the interface of two dissimilar materials, we could compute the average value of the single scattering function $W(\theta, t')$ as

$$\bar{W}(\theta) = \frac{1}{t} \int_0^t W(\theta, t') dt = \frac{4}{t \theta^4} \int_0^t dt' \frac{\sum_i N_i(t') \alpha_i^2(t) q(\theta, t')}{k^2(t')} \quad (\text{A-61})$$

However, in the Monte Carlo computer codes MCIMP and MCABLE the step sizes are adjusted at interface, such that, the equivalent step size in air is always the same and the scattering takes place in the resulting material as if it had traveled in that material. Although this is not the same as averaging the single scattering function, any errors introduced by this technique should be small due to the statistics of traveling in both directions, the number of scatterings per unit pathlength, and the averaging of the distribution functions due to differences in the electron densities of the materials over small ranges should be insignificant. Therefore, for a homogenous scatterer with no energy loss we define a characteristic angle according to Scott¹⁰ as

$$\chi_C^2 = 4\pi \frac{N\alpha^2}{k^2} t$$

$$\chi_C^2 = 4\pi e^4 z^2 Z^2 Nt/p^2 v^2 \text{ radians}^2 \text{ for heavy particles} \quad (\text{A-62})$$

and

$$\chi_C^2 = 4\pi e^4 z^2 Z(Z+1) Nt/p^2 v^2 \text{ radians}^2 \text{ for electrons} \quad (\text{A-63})$$

where $N = N_0 \rho / A$

$N_0 =$ Avogadro's number

$\rho =$ density of the scatterer in g/cm^3

$A =$ atomic weight of scatterer

$pv =$ the energy of particle in Mev

and $t =$ the step size between scattering events in centimeters.

Substituting χ_C^2 into Equation 61, we can now write the exponents in Equation 59 as

$$\Omega(\xi) - \Omega_0 = 2\chi_C^2 \int_0^\infty \frac{d\theta}{\theta^3} q(\theta) [J_0(\xi\theta) - 1] \quad (\text{A-64})$$

Following the arguments of Scott¹⁰ and Bethe¹⁴ we can approximate the above integral equation as

$$\Omega(\xi) - \Omega_0 = \frac{1}{4} \chi_C^2 \xi^2 \ln \left(\frac{\gamma^2 \chi_m^2 \xi^2}{4e} \right) \quad (\text{A-65})$$

where $\ln \gamma =$ the Euler constant 0.5772. Although the inverse Hankel transform of Equation 59 according to Equation 54 would yield the desired spatial distribution, this is obviously not a simple task. Moliere elected to break up the inverse transform by introducing a new parameter B and a new variable η as follows:

$$\Omega(\xi) - \Omega_0 = \frac{1}{4} \chi_C^2 \xi^2 \ln \left(\frac{\gamma^2 \chi_m^2 \xi^2 B}{4e B} \right) = \frac{1}{4} \chi_C^2 \xi^2 \left[\ln \frac{\gamma^2 \chi_m^2}{e B \chi_C^2} + \ln \frac{B \chi_C^2 \xi^2}{4} \right]$$

and
$$\Omega(\xi) - \Omega_0 = \frac{\eta^2}{4B} \left(\ln \frac{\gamma^2 \chi_m^2}{e \chi_C^2 B} + \ln \frac{\eta^2}{B} \right) \quad (\text{A-66})$$

where
$$\eta = \xi \chi_C B^{1/2} \quad (\text{A-67})$$

This enabled Moliere to write the first term in the spatial distribution function as a Gaussian term by setting the coefficient of the first term in the equation to minus one. That is,

$$\frac{1}{B} \ln \frac{\gamma^2 \chi_m^2}{e \chi_C^2 B} = -1 \quad (\text{A-68})$$

Solving for B, we get the transcendental equation

$$B = \ln B - .1544 + \ln \frac{\chi_C^2}{\chi_m^2} \quad (\text{A-69})$$

which according to Scott¹⁵ (1952) can be approximated by

$$B = 1.153 + 2.583 \log \frac{\chi_C^2}{\chi_m^2} \quad (\text{A-70})$$

to within 0.5% for values of χ_C^2/χ_m^2 between 100 and 10^5 .

The value χ_m^2/χ_C^2 is approximately equaled to Ω_0 as can be seen from Equation 59 if we assume $q=1$ for $\theta > \chi_m$ and zero for $\theta < \chi_m$. In equation form

$$\Omega_0 = 2x_c^2 \int_0^{\infty} \frac{q(\theta)d\theta}{\theta^3} = 2x_c^2 \int_{x_m}^{\infty} \frac{d\theta}{\theta^3} = \frac{x_c^2}{x_m^2} \quad (\text{A-71})$$

Although this value of Ω_0 is not necessary here, it will be used later in the Snyder-Scott distribution. The spatial distribution can now be written as the inverse Hankel transform of

$$\tilde{F}(\xi, t) = e^{\Omega(\eta) - \Omega_0} = e^{-\frac{\eta^2}{4} \left(1 + \frac{1}{B} \ln \frac{\eta^2}{4}\right)} \quad (\text{A-72})$$

which can be expanded into the form of

$$\tilde{F}(\xi, t) = e^{-\frac{\eta^2}{4}} \left[1 + \frac{\eta^2}{4B} \ln \frac{\eta^2}{4} + \frac{1}{2} \left(\frac{\eta^2}{4B} \ln \frac{\eta^2}{4} \right)^2 + \dots \right] \quad (\text{A-73})$$

Introducing a reduced angular variable θ

$$\text{as } \theta = \frac{\eta}{x_c B^{1/2}} \quad (\text{A-74})$$

we can write the normalized spatial distribution in terms of the normalized reduced spatial distribution as

$$2\pi F_R(\theta, t) \theta d\theta = 2\pi F(\theta, t) \theta d\theta$$

Taking the inverse Hankel transform of Equation 73 we get

$$2\pi F_R(\theta, t) = \int_0^{1/2} n dn J_0(\theta n) e^{-\frac{\eta^2}{4} \left[1 + \frac{\eta^2}{4B} \ln \frac{\eta^2}{4} + \frac{1}{2} \left(\frac{\eta^2}{4B} \ln \frac{\eta^2}{4} \right)^2 + \dots \right]} \quad (\text{A-75})$$

or

$$F_R(\theta, t) = \frac{1}{2\pi} 2e^{-\theta^2} \left[+ \frac{1}{B} F^{(1)}(\theta) + \frac{1}{B} F^{(2)}(\theta) + \dots \right] \quad (A-76)$$

where

$$F^N(\theta) = \frac{1}{N!} \int_0^\infty n^n J_0(\theta n) e^{-\frac{n^2}{4}} \left(\frac{n^2}{4} \right)^N$$

Equation 76 represents the Moliere result for the normalize spatial distribution function for particles due to multiple scatterings.

Snyder and Scott in a direct numerical integration of the inverse transform of the projected angle distribution derived analytical fits which are easily evaluated. Rather than attempt to evaluate Equation 76 in the Monte Carlo codes, we elected to evaluate the projected distribution given by Snyder and Scott¹⁰ as

$$W(\theta_R, \Omega_0) = A_1 e^{-a_1 \theta_R^2} + A_2 e^{-a_2 \theta_R^2} \quad \text{for } W > .007 W(0, \Omega_0) \quad (A-77)$$

and

$$W(\theta_R, \Omega_0) = \frac{\Omega_0}{2\theta_R^3} \left\{ 1 + \frac{11.68\Omega_0 \log(10\Omega_0)}{\theta_R^2} \right\} \quad (A-78)$$

for $W < .007 W(0, \Omega_0)$

where

$$\begin{aligned}A_1 &= [\Omega_0 (-951 + 865 \log \Omega_0)]^{-1/2} \\A_2 &= [\Omega_0 (6.3 + 10.0 \log \Omega_0)]^{-1/2} \\a_1 &= [\Omega_0 (10.96) + 4.381 \log \Omega_0]^{-1} \\a_2 &= [\Omega_0 (0.216 + 2.326 \log \Omega_0)]^{-1}\end{aligned}$$

and introduce a separate angle for the azimuthal dependence. The reduced angle θ_R is given by

$$\theta_R = \theta_p / \chi_m$$

where θ_p is the projected angle and Ω_0 is defined in Equation 71 as χ_c^2 / χ_m^2 .

DISTRIBUTION LIST

DEPARTMENT OF DEFENSE

Assist to the Sec of Def, Atomic Energy
ATTN: Exec Assist
ATTN: J. Pubell

Def Comm Engineer Ctr
ATTN: Code R123, Tech Lib
ATTN: Code R400
ATTN: Code R720, C. Stansberry

Defense Intell Agency
ATTN: DB 4C2, D. Spohn
ATTN: RTS-2A, Tech Lib
ATTN: RTS-2B

Defense Nuclear Agency
ATTN: NASF
ATTN: RAEV
ATTN: STNA
4 cys ATTN: STTI-CA

Def Tech Info Ctr
12 cys ATTN: DD

Field Command, DNA, Det 2
Lawrence Livermore National Lab
ATTN: FC-1

Field Command, Defense Nuclear Agency
ATTN: FCLMC, H. Putnam
ATTN: FCPR
ATTN: FCTT, W. Summa
ATTN: FCTXE

Interservice Nuc Wpns School
ATTN: ITV

Joint Chiefs of Staff
ATTN: J-3, Strat Opns Div

Joint Strat Tgt Planning Staff
ATTN: JLAA
ATTN: JPTM

National Communications System
ATTN: NCS-TS

National Security Agency
ATTN: R-52, O. Van Gunten
ATTN: TDL

Under Secy of Def for Rsch & Engrg
ATTN: Strat & Space Sys (OS)

DEPARTMENT OF THE ARMY

BMD Systems Command
ATTN: BMDSC-ACLIB

Fort Huachuca
ATTN: CCH-PCA-TR

US Army Comm, Elect Command
ATTN: DRDCO-SE1

DEPARTMENT OF THE ARMY (Continued)

Harry Diamond Laboratories
ATTN: DELHD-NW, J. Rosado
ATTN: DELHD-NW-E
ATTN: DELHD-NW-EA
ATTN: DELHD-NW-EB
ATTN: DELHD-NW-EC
ATTN: DELHD-NW-ED
ATTN: DELHD-NW-EE
ATTN: DELHD-NW-P
ATTN: DELHD-R
ATTN: DELHD-TA-L, Tech Lib
ATTN: DELHD-TD
ATTN: DELHD-TF
2 cys ATTN: DELHD-NW-RC

US Army Armor Ctr
ATTN: Tech Lib

US Army Ballistic Rsch Lab
ATTN: DRDAR-BLB, W. Van Antwerp
ATTN: DRDAR-BLE

US Army Communications Command
ATTN: ATSI-CD-MD
ATTN: CC-LOG-LEO
ATTN: CC-OPS-OS
ATTN: CC-OPS-PD

US Army Communications Sys Agency
ATTN: CCM-AD-SV
ATTN: CCM-RD-T

US Army Electronics R&D Command
ATTN: DELSD-L, W. Werk

US Army Engineer Div
ATTN: HNDED-SR
ATTN: T. Bolt

US Army Intel Threat Analysis Det
ATTN: Admin Officer

US Army Intell & Sec Cmd
ATTN: Tech Lib

US Army Materiel Sys Analysis Actvy
ATTN: DRXSY-PO

US Army Nuc & Chem Agcy
ATTN: MONA-WE

US Army Test & Eval Comd
ATTN: DRSTE-CM-F
ATTN: DRSTE-CT-C

US Army Training & Doctrine Comd
ATTN: ATCD-Z

US Army White Sands Missile Range
ATTN: STEWS-TE-N, K. Cummings

USA Missile Command
ATTN: AMSMI-SF, G. Thurlow
ATTN: Documents Section
ATTN: DRCPM-PE-EA, W. Wagner
ATTN: DRCPM-PE-EG, W. Johnson

DEPARTMENT OF THE NAVY

Naval Air Systems Command
ATTN: AIR 350F

Naval Electronic Systems Command
ATTN: PME 117-21

Naval Ocean Systems Center
ATTN: Code 54, C. Fletcher

Naval Ordnance Station
ATTN: Standardization Div

Naval Postgraduate School
ATTN: Code 1424, Library

Naval Rsch Laboratory
ATTN: Code 2000, J. Brown
ATTN: Code 2627, D. Folen
ATTN: Code 4700, W. Ali
ATTN: Code 4701, I. Vitokovitsky
ATTN: Code 4760, R. Grieg
ATTN: Code 6624
ATTN: Code 6750

Naval Surface Wpns Ctr
ATTN: Code F30
ATTN: Code F32, E. Rathbun

Naval Wpns Ctr
ATTN: Code 343, FKA6A2, Tech Svcs

Naval Wpns Eval Facility
ATTN: Code AT-6

Naval Wpns Support Ctr
ATTN: Code 11E

Ofc of the Dep Ch of Naval Ops
ATTN: NOP 981N1

Strategic Systems Project Office
ATTN: NSP-2301, M. Meserole
ATTN: NSP-2701
ATTN: NSP-27334
ATTN: NSP-43, Tech Lib

DEPARTMENT OF THE AIR FORCE

Aeronautical Systems Div
ATTN: ASD/ENSSA
ATTN: ASD/YEYF

Air Force Aeronautical Sys Div
2 cys ATTN: ASD/ENACE, J. Corbin

Air Force Inst of Technology, Air University
ATTN: ENA, G. Baker

Air Force Wpns Laboratory
ATTN: NT
ATTN: NTYEE, C. Baum
ATTN: NTYEP, W. Page
ATTN: SUL

Air Logistics Command
ATTN: OO-ALC/MM
ATTN: OO-ALC/MMEDO, L. Kidman
ATTN: OO-ALC/MMETH, P. Berthel

DEPARTMENT OF THE AIR FORCE (Continued)

Air University Library
ATTN: AUL-LSE

Ballistic Missile Office/DAA
ATTN: ENSN, W. Clark
ATTN: ENSN, W. Wilson
ATTN: M. Stapanian
2 cys ATTN: ENSN

Dep Ch of Staff, Rsch, Dev & Acq
ATTN: AF/RDQI

Electronic Systems Div
ATTN: SCS-1E

Foreign Technology Div
ATTN: TQTD, B. Ballard

Rome Air Dev Ctr
ATTN: TSLD

Space Command
ATTN: DEE

Space Division
ATTN: IND

Strategic Air Command
ATTN: INAO
ATTN: NRI/STINFO
ATTN: XPFS
ATTN: XPQ

DEPARTMENT OF ENERGY

Department of Energy
Albuquerque Opns Office
ATTN: CTID
ATTN: WSSB

OTHER GOVERNMENT AGENCIES

Central Intell Agcy
ATTN: OSWR/NED

Dept of Transportation, Fed Aviation Admin
ATTN: SEC Div, ASE-300

Fed Emergency Mgmt Agcy
ATTN: OPIR, M. Murtha
ATTN: SL-EM, J. Hain

NORAD
ATTN: NORAD/J5YX

DEPARTMENT OF ENERGY CONTRACTORS

University of California
Lawrence Livermore National Lab
ATTN: L-10, H. Kruger
ATTN: L-13, D. Meeker
ATTN: L-153, E. Miller
ATTN: L-156, H. Cabayan
ATTN: L-97, T. Donich
ATTN: Tech Info Dept Library

Los Alamos National Laboratory
ATTN: MS670, J. Malik

DEPARTMENT OF ENERGY CONTRACTORS (Continued)

Sandia National Laboratories
ATTN: G. Yonas
ATTN: M. Morris
ATTN: T. Martin

DEPARTMENT OF DEFENSE CONTRACTORS

Aerospace Corp
ATTN: I. Garfunkel
ATTN: J. Reinheimer
ATTN: Library
ATTN: R. Crolius

Agbabian Associates
ATTN: Library

Allied Corp
ATTN: Doc Control

Analytical Systems Engineering Corp
ATTN: M. Nucefora

AVCO Systems Div
ATTN: Library, A830

Battelle Memorial Institute
ATTN: E. Leach

BDM Corp
ATTN: Corporate Lib
ATTN: S. Clark
ATTN: W. Sweeney

BDM Corp
ATTN: Library

Boeing Co
ATTN: D. Kemle
ATTN: J. Dicome, Org 2-3744, M/S 47-36
ATTN: Kent Tech Library

Boeing Military Airplane Co
ATTN: C. Sutter

Booz-Allen & Hamilton, Inc
ATTN: R. Chrisner
ATTN: Tech Lib

Calspan Corp
ATTN: R. Thompson

Calspan Corp
ATTN: Library

Charles Stark Draper Lab, Inc
ATTN: K. Fertig
ATTN: TIC MS 74

Cincinnati Electronics Corp
ATTN: L. Hammond

Computer Sciences Corp
ATTN: A. Schiff

Dikewood Corp
ATTN: Tech Lib for D. Pirio
ATTN: Tech Lib

Dikewood Corp
ATTN: K. Lee

DEPARTMENT OF DEFENSE CONTRACTORS (Continued)

E-Systems, Inc
ATTN: J. Moore

Eaton Corp
ATTN: E. Karpen

EG&G Wash Analytical Svcs Ctr, Inc
ATTN: C. Giles

Ford Aerospace & Communications Corp
ATTN: H. Linder

General Dynamics Corp
ATTN: Rsch Lib

General Dynamics Corp
ATTN: Rsch Lib

General Electric Co
ATTN: D. Nepveux
ATTN: J. Peden

General Electric Co
ATTN: C. Hewison

General Electric Co
ATTN: Tech Lib

General Rsch Corp
ATTN: Tech Info Ofc

Georgia Institute of Technology
ATTN: RES & SEC Coord for H. Denny

Grumman Aerospace Corp
ATTN: L-01 35

GTE Communications Products Corp
ATTN: A. Novenski
ATTN: D. Flood
ATTN: J. Waldron
ATTN: M. Snow

GTE Government Systems Corp
ATTN: L. Lesinski

Harris Corp
ATTN: A. Strain
ATTN: V Pres & Mgr Prgms Div

Hazeltine Corp
ATTN: J. Okrent

Honeywell, Inc
ATTN: R. Johnson
ATTN: S&RC Library

Honeywell, Inc
ATTN: S. Graff
ATTN: W. Stewart

Hughes Aircraft Co
ATTN: CTDC, 6/E110
ATTN: K. Walker

Hughes Aircraft Intl Svc Co
ATTN: A. Narevsky, 532/C332

Institute for Def Analyses
ATTN: Tech Info Svcs

DEPARTMENT OF DEFENSE CONTRACTORS (Continued)

IIT Rsch Institute
ATTN: I. Mindel
ATTN: J. Bridges

IRT Corp
ATTN: B. Williams
ATTN: N. Rudie

JAYCOR
ATTN: D. Higgins

JAYCOR
ATTN: E. Wenaas
ATTN: R. Stahl

JAYCOR
ATTN: Library

Kaman Sciences Corp
ATTN: A. Bridges
ATTN: F. Shelton
ATTN: N. Beauchamp
ATTN: W. Rich

Kaman Sciences Corp
ATTN: E. Conrad

Kaman Tempo
ATTN: DASIAC
ATTN: R. Rutherford
ATTN: W. McNamara

Kaman Tempo
ATTN: DASIAC

Litton Systems, Inc
ATTN: MS 64-61/E, Eustis

Litton Systems, Inc
ATTN: J. Skaggs

Lockheed Missiles & Space Co, Inc
ATTN: Tech Info Ctr

Lockheed Missiles & Space Co, Inc
ATTN: D. Nishida, Dept 85-76
ATTN: H. Thayn
ATTN: L. Rossi
2 cys ATTN: S. Taimuty, Dept 81-74/154

Martin Marietta Corp
ATTN: J. Casalese
ATTN: M. Griffith

McDonnell Douglas Corp
ATTN: T. Ender, 33/6/618

McDonnell Douglas Corp
ATTN: S. Schneider
ATTN: Tech Lib Svcs

McDonnell Douglas Corp
ATTN: M. Potter
ATTN: R. Twomey, MS/36-43

Metatch Corp
ATTN: W. Radasky

Mitre Corp
ATTN: M. Fitzgerald

DEPARTMENT OF DEFENSE CONTRACTORS (Continued)

Mission Rsch Corp
ATTN: EMP Group
ATTN: J. Gilbert
2 cys ATTN: E. Kalasky
5 cys ATTN: Doc Control

Mission Rsch Corp
ATTN: A. Chodorow
ATTN: D. Gardner
ATTN: M. Scales

Mission Rsch Corp
ATTN: J. Lubell
ATTN: R. Curry
ATTN: W. Stark
ATTN: W. Ware

Mission Rsch Corp
ATTN: J. Erler
ATTN: V. Van Lint

Norden Systems, Inc
ATTN: Tech Library

Northrop Corp
ATTN: B. Ahlport

Pacific-Sierra Rsch Corp
ATTN: H. Brode, Chairman SAGE

Palisades Inst for Rsch Svcs, Inc
ATTN: Records Supervisor

Physics International Co
ATTN: Doc Control

R&D Associates
ATTN: C. Knowles
ATTN: Doc Control
ATTN: P. Haas
ATTN: W. Karzas

Rand Corp
ATTN: B. Bennett

Raytheon Co
ATTN: G. Joshi

Raytheon Co
ATTN: H. Flescher

RCA Corp
ATTN: G. Brucker

Rockwell International Corp
ATTN: D/243-068, 031-CA31
ATTN: J. Erb
ATTN: V. Michel

Rockwell International Corp
ATTN: B. White

Rockwell International Corp
ATTN: F. Shaw

Rockwell International Corp
ATTN: B-1 Div, TIC, BA0B

S-CUBED
ATTN: A. Wilson

DEPARTMENT OF DEFENSE CONTRACTORS (Continued)

Science & Engrg Associates, Inc
ATTN: V. Jones

Science Applications Intl Corp
ATTN: W. Chadsey

Singer Co
ATTN: Tech Info Ctr

Sperry Corp
ATTN: Tech Library

Sperry Corp
ATTN: D. Schow

SRI International
ATTN: A. Whitson
ATTN: E. Vance

Teledyne Brown Engineering
ATTN: F. Leopard
ATTN: J. Whitt

DEPARTMENT OF DEFENSE CONTRACTORS (Continued)

Texas Instruments, Inc
ATTN: D. Manus
ATTN: Tech Lib

Transients Limited Corp
ATTN: D. Clark

TRW Electronics & Defense Sector
ATTN: H. Holloway
ATTN: L. Magnolia
ATTN: O. Adams

TRW Electronics & Defense Sector
ATTN: R. Kitter
ATTN: R. Mortensen

Varian Associates, Inc
ATTN: H. Jory

Allied Corp
ATTN: M. Frank

END

FILMED

1-86

DTIC